Wave-Particle Studies in the Ion Cyclotron and Lower Hybrid Range of Frequencies in Alcator C-Mod

P.T. Bonoli, R. Parker, S.J. Wukitch, Y. Lin, M. Porkolab, J.C. Wright, E. Edlund, T. Graves, L. Lin, J. Liptac, A. Parisot, A.E. Schmitt, V. Tang, W. Beck, R. Childs, M. Grimes, D. Gwinn, D. Johnson, J. Irby, A. Kanojia, P. Koert, S. Marazita, E. Marmar, D. Terry, R. Vieira, G. Wallace, J. Zaks

Plasma Science and Fusion Center, MIT, Cambridge, MA, 02139 (USA)

— • —

S. Bernabei, C. Brunkhorse, R. Ellis, E. Fredd, N. Greenough, J. Hosea, C.C. Kung, G.D. Loesser, J. Rushinski, G. Schilling, C.K. Phillips, J.R. Wilson

Princeton Plasma Physics Laboratory, Princeton University, Princeton, NJ, 08543 (USA)

— • —

R.W. Harvey

CompX, Del Mar, CA, 92014 (USA)

— • —

C.L. Fiore, R. Granetz, M. Greenwald, A.E. Hubbard, I.H. Hutchinson, B. Labombard, B. Lipschultz, J. Rice, J.A. Snipes, J. Terry, S.M. Wolfe, and the Alcator C-Mod Team

Plasma Science and Fusion Center, MIT, Cambridge, MA, 02139 (USA)

Plasma Science and Fusion Center
Massachusetts Institute of Technology
Cambridge MA 02139 USA

December 2005

"Wave-Particle Studies in the Ion Cyclotron and Lower Hybrid Range of Frequencies in Alcator C-Mod"

P.T. Bonoli, R. Parker, S.J. Wukitch, Y. Lin, M. Porkolab, J.C. Wright,
E. Edlund, T. Graves, L. Lin, J. Liptac, A. Parisot, A.E. Schmitt, V. Tang,
W. Beck, R. Childs, M. Grimes, D. Gwinn, D. Johnson, J. Irby, A. Kanojia, P. Koert,
S. Marazita, E. Marmar, D. Terry, R. Vieira, G. Wallace, J. Zaks

Plasma Science and Fusion Center, MIT, Cambridge, MA, 02139 (USA)

S. Bernabei, C. Brunkhorse, R. Ellis, E. Fredd, N. Greenough, J. Hosea, C.C. Kung, G.D. Loesser, J. Rushinski, G. Schilling, C.K. Phillips, J.R. Wilson

Princeton Plasma Physics Laboratory, Princeton University, Princeton, NJ, 08543 USA

R.W. Harvey
CompX, Del Mar, CA, 92014 (USA)

C.L. Fiore, R. Granetz, M. Greenwald, A.E. Hubbard, I.H. Hutchinson,
B. Labombard, B. Lipschultz, J. Rice, J.A. Snipes, J. Terry, S.M. Wolfe, and the
Alcator C-Mod Team

Plasma Science and Fusion Center, MIT, Cambridge, MA, 02139 (USA)

ABSTRACT

This paper reviews the physics and technology of wave-particle interaction experiments in the ion cyclotron range of frequencies (ICRF) and the lower hybrid range of frequencies (LHRF) on the Alcator C-Mod tokamak. Operation of fixed frequency (80 MHz) and tunable (40 – 80 MHz) ICRF transmitters and the associated transmission system is described. Key fabrication issues that were solved in order to operate a four strap ICRF antenna in the compact environment of C-Mod are discussed in some detail. ICRF heating experiments utilizing the hydrogen (H) and (He^3) minority heating schemes are described and data is presented demonstrating an overall heating efficiency of 70 – 90% for the (H) minority scheme and somewhat lower efficiency for (He^3) minority heating. Mode conversion electron heating experiments in $D(He^3)$, $D(H)$, and $H(He^3)$ discharges are also reported as well as simulations of these experiments using an advanced ICRF full-wave solver. Measurements of mode converted ion cyclotron waves (ICW) and ion Bernstein waves (IBW) using a phase contrast imaging (PCI) diagnostic are presented and compared with the predictions of a synthetic diagnostic that utilizes wave electric fields from a full-wave solver. The physics basis of the LH current profile control program on Alcator C-Mod is also presented. Computer simulations using a 2D (velocity space) Fokker Planck solver indicate that about 200 kA of LH current can be driven in low density H-mode discharges on C-Mod with about 3 MW of LHRF power. It is shown that this off-axis LH current drive can be used to create discharges with non-monotonic profiles of the current density and reversed shear. An advanced tokamak operating regime near the ideal no-wall β-limit is described for C-Mod, where about 70% of the current is driven through the bootstrap effect. The LH power is coupled to C-Mod through a waveguide launcher consisting of four rows (vertically) with 24 guides per row (toroidally). A detailed description of the LH launcher fabrication is given in this paper along with initial operation results.

I. INTRODUCTION

Radio-frequency power in the ion cyclotron range of frequencies (ICRF) has been the sole means of auxiliary plasma heating available on Alcator C-Mod. Thus a detailed understanding of the ICRF wave-particle interaction is needed to ensure success of the overall C-Mod program. A wide range of operating magnetic field strengths ($B_0 = 2.6 - 8.0$ T) coupled with the availability of both fixed frequency (80 MHz) and tunable RF sources (40 – 80 MHz) makes it possible to investigate a variety of minority ion heating schemes at the fundamental and second harmonic of the minority ion cyclotron frequencies of hydrogen (H) and Helium-3 (^{3}He). The majority species in these plasmas is typically deuterium (D). Mode conversion of the injected fast magnetosonic wave to short wavelength modes [ion Bernstein waves (IBW) and ion cyclotron waves (ICW)] has also been studied extensively in two species (D-^{3}He) and three species plasmas (D-^{3}He-H). A thorough understanding of wave-particle processes in the ICRF may be crucial to the eventual success of the tokamak as a fusion reactor. Minority heating is a likely candidate for bulk plasma heating in burning plasmas and ICRF mode conversion processes may provide a means for localized current and pressure profile control in achieving high performance modes of operation. In order to better understand and supplement these experimental investigations on Alcator C-Mod a suite of advanced ICRF simulation codes have been developed and implemented on massively parallel computing platforms.

More recently a lower hybrid current drive (LHCD) system has been installed on Alcator C-Mod that utilizes 3 MW of LHRF source power at 4.6 GHz. This tool will be used for off-axis current profile control in order to access improved confinement regimes in C-Mod. The LH launcher consists of a phased array of 96 waveguides placed in four rows (vertically) with 24 waveguides per row. The launcher is capable of producing directional spectra in the range $2 \leq n_{//} \leq 3$, with real time phase control. [Here $n_{//}$ is the parallel refractive index of the coupled LH waves.] Sophisticated models for LH current drive have been used in conjunction with ideal MHD equilibrium and stability

calculations in order to better understand and optimize these upcoming LH current profile control experiments.

The plan of this paper is as follows. Engineering and design issues of the ICRF transmission system and antennas are discussed in Section II. Physics studies of ICRF minority heating on Alcator C-Mod are discussed in Section III and physics studies of ICRF mode conversion are described in Sec. IV, including a review of detailed computer simulations of these experiments. In Section V, we present simulations of planned lower hybrid (LH) current profile control experiments on Alcator C-Mod. The LH launcher and transmission line system that was fabricated to perform these experiments is described in detail in Section VI, as well as results from initial LH launcher operation. Finally, a summary is given in Section VII.

II. HIGH POWER ICRF SYSTEM

A. Introduction

Although available sources, transmission networks, and coupling structures are based upon fairly well known principles, the severe high power and harsh plasma conditions typical of C-Mod discharges present serious challenges for ICRF systems. Thus both physics and technological issues involving the development of suitable transmitters, matching networks, and launchers are important for the overall success of the C-Mod experiment. The transmitters are based on FM radio broadcast transmitters with nominal 2 MW output power, and the transmission network utilizes standard coax with Teflon insulating supports, including phase shifters and stub tuners for load matching purposes. Three antennas, including two 2-strap and one 4-strap antenna, have delivered up to 6 MW of power with antenna surface power densities in excess of 10 MW/m^2 with low impurity and density production.

B. Transmitters

The C-Mod ICRF plant consists of four modified so-called FMIT transmitters built by Continental Electronics in the 1980s (originally for the Fusion Materials Irradiation Test Facility). All the transmitters have been modified to increase the output power from 0.65 MW to 2 MW. Two of the transmitters FMIT #1 and #2 are operated at a fixed frequency of 80 MHz and two other units, FMIT #3 and #4 operate from 40-80 MHz. The primary operation frequency for FMIT#3 and #4 is 78 MHz with more limited operation time at 50 and 70 MHz (dictated by the physics program) and the transmitters have been operated into a fixed 50 Ω load for up to a 5 second long pulse. The transmitters are a three stage amplifier where the final amplifier stage utilizes a 4CM2500KG EIMAC tetrode operating in class C for 2 MW output (gain ~13 dB). We have also utilized two lower power tubes over the course of C-Mod operation: the 8973 (~1 MW output) and x2242 (~1.5 MW output). The driver stage uses a more conventional broadcast tetrode, an EIMAC 4CW100000E, with an output of ~100 kW and the initial power amplifier (IPA) is a 5 kW triode (EIMAC 3CW5000A7) based class AB amplifier.

We should note here a couple of critical features of the 4CM2500KG to consider in its operation. Tube arc protection is an important issue because of delicate control and because screen grids are made of pyrolytic graphite having a dissipation rating of 8 kW and 20 kW, respectively.[1] This is substantially more power dissipation capability than the 2.0 kW (control) and 7.5 kW (screen) for conventional wire grids of the x8973 above;[1] however they are somewhat less rugged. During an arc, the stored energy in the anode and screen power supply should be dumped to ground to limit the energy dissipated into the arc to less than 50 J. Further, the voltage applied to the screen and grid should be limited by external spark gaps, set to ~ 2 kV in our system, to avoid excessive voltage during off-normal events. After adding screen crowbar circuits and external spark gaps to protect the grid screens, the tube lifetime increased from ~1000 filament hours to 2500-2700 filament hours. The postmortem investigation of failed tubes SN#PBC-9 and SN#FKH-56 revealed a stem leak and localized anode melting in

both tubes. One tube PBC-9 had a full triangle missing from the grid that appeared to align with the localized melt damage and is likely the reason for the melt. In the other tube FKH-56, the screen and grid have a greenish discoloration resulting from a water leak (likely at the localized melting on the anode). There are a couple of bars missing from the screen and at least one shows evidence of delamination/flaking, but it is unclear whether this arose after or before the water leak. Since we have only postmortem data on these rebuilt tubes and have data from a limited number of tubes, we have not identified a design or operation dependent failure mechanism. Although the tubes can be rebuilt (typically ~3 times), the delivery time is typically 8-10 months for the first tube and another month for each tube thereafter. Because the tubes are manufactured infrequently, some problem in the manufacturing of the tubes is experienced regularly but eventually the problems have been solved. Another issue is that the plate impedance at high frequency (~80 MHz) is higher than expected. We have implemented, on two transmitters, a modification to the lower part of the output cavity near the tube to lower the plate impedance. This has allowed 2.5 MW output into dummy load and 2 MW into plasma. Finally, parasitic oscillations have been observed in the 800-2000 MHz range that can lead to localized heating of the screen and/or anode and can result in premature loss of the tube. Parasitic oscillations often occur at low power and can be controlled through the use of ferrites glued onto the tube itself between the screen and grid contact and ferrite wedges built into the tube socket. The location of the shorting elements depends upon the particular tube installed and the operating frequency. For 70 and 78 MHz operation, the rods are fully inserted but for 50 MHz these rods are fully retracted.

In the future, we would like to pursue two upgrades to the transmitters: higher power operation and conversion of the fixed frequency transmitters to 40-80 MHz transmitters. The present ICRF power supplies built by Uptegraff are rated at 155 A (140 A at 28 kV and 15 A at 16 kV) for 10 sec, with 17 minutes between pulses. To obtain full transmitter performance, the supply needs to provide total current of ~190 A (~170 A for the final and ~15 A for the driver). Furthermore, the final output cavity would require an additional modification to lower the plate impedance to maintain the screen dissipation below 20 kW. To improve output power, the IPA should be upgraded from 5 kW to 10

kW because this stage has proven to saturate first and provides the highest gain. Finally, the screen power supplies are marginal for the present power output and would require an upgrade for higher power operation. Under some experimental conditions, the power delivered to the plasma has been limited by the power supplies. Increasing the frequency range of the fixed frequency transmitters through the addition of tunable cavities would increase the flexibility of the system to allow tailoring of the power deposition profiles for a wider array of plasma conditions.

C. Transmission Network

The primary function of the transmission network is to transform the antenna load to match the load expected by the transmitters, 50 Ω resistive in our case. The antenna input impedance is dominated by the reactive component with a small real component, much smaller than the transmission line impedance. The impedance transformation is accomplished by the use of a mechanical phase shifter and stub tuner. The system is tuned between discharges assuming that the subsequent discharge will be similar to the previous one. This may appear to be a rather naïve approach, but as shown in previous work, the plasma loading falls into a rather small region of the Smith chart and this technique has worked reasonably well.[2] Another function of the network system is to divide the power and control the relative phase between radiating elements.

To further complicate the matching problem, the antenna input impedance is variable with changes of order < 1 msec. Compared with other experiments, the loading resistance on C-Mod is quite high and the load variations are less severe, allowing rather simple solutions. Two approaches to make the system load tolerant have been pursued. The first is the so-called conjugate T configuration, where the input impedance of two independent elements is transformed in such a fashion as to allow their variation to cancel at the conjugate T. Modeling indicated that this configuration could result in current asymmetries between the two elements and this was confirmed in experimental tests on the E antenna. Interestingly, the current imbalance did not result in an increase in density or impurity production and the antenna operated with the same heating effectiveness as

an identical antenna with a standard resonant loop transmission network[3]. Another complication for the C-Mod antennas is the rather strong coupling between the antenna elements that effectively prevented the simple load tolerant configuration from delivering load tolerant behavior. The influence of coupling has been further investigated by other authors, who found that an appropriate configuration can be designed, but due to physical constraints this cannot be implemented on C-Mod.[4]

Another method uses active tuning elements based upon ferrite loaded strip lines. Here the electrical length of shorted stubs can be controlled by an applied magnetic field of order 3-5 kG. The response of the stub is determined by the inductance of the associated magnets and their power supplies. These experiments were inspired by earlier work done at GA and IPP-Garching and initial experiments in fact will use the same stubs built for GA.[5,6] A potential limitation is the power dissipated in the ferrite material that is a very sensitive function of the antenna reflection coefficient. In typical C-Mod operation, the reflection coefficient is between 0.7-0.85 resulting from the high plasma loading of these antennas (significantly higher than other current experiments like DIII-D, JET, or ASDEX-U). If necessary, the reflection coefficient could be reduced further through the use of quarter wavelength transformers as shown in previous experiments on C-Mod.

D. ICRF Antennas

In C-Mod, one of the primary tasks has been to develop antennas that can operate up to 10 MW/m^2 in power density while limiting the plasma density rise and impurity production associated with antenna operation. The C-Mod antenna designs have incorporated available experimental experience and theoretical models. For the 2-strap (D and E) antennas, the antenna design[7,8] was similar to successful antennas utilized on a TFTR with shields to cover the radial feeders and Faraday screen elements aligned with the total magnetic field. However, a major concern was runaway self-sputtering, particularly from the Faraday screen, due to the high plasma densities and metallic plasma facing components. These antennas have achieved power densities of ~10 MW/m^2 without significant impurity production problems. To increase the auxiliary

power and allow for directed wave launch, a third antenna, J antenna,[9,10] was added in 1998 that was to achieve the same 10 MW/m^2 power densities through a single port with 4 current straps. The increase from 2 to 4 straps meant the loss of antenna symmetry (straps 1 and 4 have one immediate neighbor while 2 and 3 have two) that greatly complicates the antenna design and operation.

In C-Mod, antenna performance has been primarily limited by voltage breakdown and impurity generation. The incremental density increase associated with ICRF operation has been small and becomes negligible once the machine and antenna are conditioned. Voltage breakdowns can be classified as either high or low voltage breakdown. The former is an arc that develops at a high voltage point and results in a detuning of the transmission network. The voltage at which arcs occur is complicated by the many effects including geometry, surface preparation, the magnetic field orientation, plasma generated ionizing radiation and energetic neutrals, high edge neutral pressure ($\sim$0.1-1 mTorr in C-Mod), and machine conditioning (boronization leaves a soft gas-laden coating.) Low voltage breakdowns result from plasma formation and can be difficult to detect. When the RF E-field is parallel to the tokamak B-field (E$\parallel$B), the high voltage electrical breakdown limit has been inferred to be as low as E$\sim$1.5 MV/m, and at least E$\sim$3.5 MV/m for E$\perp$B during plasma operation. These limits are consistent with earlier breakdown studies that suggested that E-fields of $\sim$0.9 MV/m and 5 MV/m could be supported where E$\parallel$B and E$\perp$B, respectively[11] and the operational experience of other experiments.[12] In the presence of high neutral pressure (0.4-1 mtorr) and magnetic fields, the multipactor susceptibility is modified such that the typical RF voltages cannot be applied.[13]

Impurity and density production have been recurrent issues for a number of ICRF experiments including C-Mod.[14,15,16,17,18,19,20,21,22,23] To overcome these issues, Faraday screens (FS) and protection limiters have been added that improved voltage handling and heating efficiency. Optically opaque FS's limit the plasma induced reactive impedance, a change that can be beneficial when designing the matching network, and a FS increases the effective electrical length of an antenna (the larger the number of FS rod elements the

longer the electrical length of the antenna). However, the trade-offs are that the FS's themselves may become a source of impurities.[24,25] In addition, the FS's are expensive to build due to the special materials needed to withstand high heat loads and large disruption forces. In C-Mod, we have used metallic and insulating limiters to limit the plasma density at the FS. With the Mo limiters, core Mo content was found to scale with RF power and the primary impurity source was identified as the antenna limiters rather than the FS.[23]

E. ICRF Antenna Description

The two-strap (D and E) antenna design[7,8] is rather simple and operates in so-called dipole phase with shielded radial feed lines and Faraday screen elements aligned with the total field as shown in Fig. 1. The D and E antennas have end-fed, center grounded current straps and 30 Ω strip line vacuum transmission lines (VTL) where the RF E-field is perpendicular to the tokamak B-field everywhere except at the transition from the vacuum feedthrough to strip line. The Faraday screen is ~27% optically transparent and the elements are 0.95 cm diameter Cu-plated (4-8 μm) Inconel 625 rods coated with TiCN on the D antenna and B_4C on the E antenna, which are welded to the antenna box at both ends. The tokamak plasma limiter, private antenna limiters, Faraday screen, and antenna straps are at mid-plane major radius (R): 90.5 cm, 91.3 cm, 91.7 cm, and 93.5 cm, respectively. The strap separation is 25.75 cm on center and the straps are 10 cm wide. For the so-called dipole phasing, these antennas have a toroidal mode number (n_ϕ) spectrum peaked at ±10 ($k_{||} \approx \pm 11$ m^{-1} at the antenna straps).

The J antenna[9,10] is a compact 4-strap unit that utilizes a folded strap vacuum strip line for the antenna feeds and a more open Faraday screen and antenna box for an improved current spectrum, as shown in Fig. 2. For the J antenna, the VTL has evolved from a combination of 4" coaxial transmission line and parallel plate transmission line to a fully parallel plate design (except for the transition region from the vacuum feedthroughs to the parallel plate). The Faraday screen is 50% optically transparent and oriented parallel to the toroidal direction. The FS rods are grounded at one end and the other ends have

resistive ceramic washers (0.1 Ω impedance to ground) to minimize disruption current loads. The private antenna limiters, Faraday screen, and straps are at nearly identical positions as the other antennas: R=91.2 cm, R=91.8 cm, and R=93.6 cm, respectively. The current straps are separated by 18.6 cm on center and the straps are 8 cm wide. With straps #1-#3 and #2-#4 connected in phase, the antenna can be run with so-called dipole phasing ($n_\phi=\pm13$) or monopole phasing ($n_\phi=\pm4$). With straps #1-#3 and #2-#4 connected out of phase, the antenna phase can be either heating phase (0-π-π-0 and $n_\phi=\pm10$) or $\pm90°$ phasing (0-$\pm\pi/2$-π-$\pm3\pi/2$ and $n_\phi=\pm7$), where the +90° and -90° phasing launches waves directed co- and counter to the tokamak plasma current, respectively.

The J antenna evolved from the original design to the present one as a result in an effort to improve its overall performance.[9,10] First operation had a power limit resulting from impurity generation events (injections) at ~4.7 MW/m^2 resulting from modest voltage differences between antenna protection tiles.[10] These events were eliminated by electrically connecting the tiles; furthermore, shields were installed to interrupt the arc path between the ceramic washers and the current straps. Arcing in the VTL and antenna strap prevented high power operation due to the reduced voltage handling where the RF electric field is parallel to the tokamak magnetic field. To eliminate the Mo source and to prevent formation of RF sheaths, from particularly in the current drive phasing, insulating BN tiles (AXO5 grade from Saint-Gobain Advanced Ceramics) were installed to replace the Mo tiles. To obtain maximum power with insulating limiters, the metal-BN interfaces (fasteners and structure) had to be shielded from direct plasma contact; otherwise, severe impurity events occurred at this interface as evident in the melt damage found post-operation. Ultimately, the BN tiles proved to be too fragile (the supporting structure response to the disruption forces was sufficient to cause the BN to fracture) and the antenna was retrofitted with metallic limiters, resulting in tolerable impurity generation characteristics. The final modification to the antenna was RF grounding of the back plate. The long ground connection length resulted in a low but sufficient RF voltage to support local plasma formation. This plasma would etch the stainless steel vacuum vessel and inconel back plate of the J antenna. Simple vacuum compatible by-pass

capacitors (25 0.01 μF capacitors) have proven to be effective for limiting the RF voltage.

Although the J antenna performance has improved through these many modifications, there are conditions under which the antenna performance degrades or improves. An example of degraded voltage handling is low (<0.4 MA) plasma current operation. In contrast, in He discharges, the voltage handling appears to be improved compared to deuterium discharges. These examples of degraded or improved voltage handling may allow further insight into the physics of ICRF antenna voltage handling and will be addressed in future work.

F. System Protection

To prevent damage to high power vacuum tubes, transmission lines, and antennas, several protection circuits have been implemented. The primary antenna protection circuit is arc detection through the ratio of reflected power to forward power that is set to <25%. We have found that setting the trip level to even 30% resulted in arc events that survived for 280 μsec. Furthermore, digitizing the forward and reflected power at high frequency, ~250 kHz, has proven to be indispensable for diagnosing the off normal events. In addition, the phase relation or phase balance between antenna elements with hardware determined phase relationship is monitored for off normal phase changes in order to detect series arcs or low voltage arcs. Our only anecdotal confirmation for the need for this type of detection is that the only time we have damaged a strap of the D and E antennas is when one of these phase balance detectors was broken. The resulting damage had little resemblance to typical high voltage arc damage and more akin to spread of material from a discharge. The damaged section of line was thought to be in a region of relatively low voltage. To protect the feedthroughs from excessive voltage, we monitor the voltage near the voltage maximum and limit it to <45 kV. We have implemented to varying degrees, high voltage and high screen current limiting feedback to limit the voltage and screen current by reducing the injected power. For the most part, these so-called roll-back circuits have been unnecessary during routine operation. During

plasma operation, a video view of the antenna has also been important to determine if an impurity event is the result of an antenna-plasma interaction, and to avoid such events in subsequent discharges

III. ICRF MINORITY HEATING IN D(H) AND D(^{3}HE) PLASMAS

A. Fundamental hydrogen minority heating

Hydrogen minority ion cyclotron damping has been used to produce some of the highest stored energies ever achieved in Alcator C-Mod.[26,27,28] Detailed understanding of minority heating has emerged as a result of a close comparison between experiment, theory, and simulation. In the H-minority heating scheme in a deuterium majority plasma, the single pass absorption is expected from theory to be high since the left circularly polarized component of the fast wave is no longer shielded by the plasma ions[29,30] $[(E_+ / E_y)^2 = 1]$. Thus the minority ions resonate strongly with the injected fast wave.

An example of an ICRF heated discharge at B_T=5.4 T, I_P=1.0 MA is shown in Fig. 3. The confinement enhancement factor $H = \tau_E / \tau_{ITER89}$ reaches a value of 1.9, relative to the ITER89 H-mode scaling[31] and the normalized beta is $\beta_N = \beta/(I/aB =1.6$, with the central electron temperature reaching 4 keV at the top of the sawtooth. Even at this high RF power level, the radiated power is well controlled through wall conditioning (boronization). A second example of this heating from an earlier campaign is shown in Fig. 4 where 2.8 MW of ICRF power at 80 MHz was injected from the D- and E- two strap antennas into a discharge at 5.3T and 1.0 MA. The plasma developed into an enhanced D_α H-mode with high central density $[n_e(0) \cong 4 \times 10^{20}$ m$^{-3}]$ and temperature $[T_e(0) = 3.9$ keV and $T_i(0) = 3.0$ keV]. The stored energy was 200 kJ corresponding to $\beta_N = 1.5$ and a confinement enhancement factor of H=2. Large sawteeth measured on the central electron temperature channel of a nine channel electron cyclotron emission grating polychromator (GPC) system[32] indicate that significant power from the energetic ICRF minority tail is slowing down via electron drag. Analysis of the ICRF wave propagation and absorption physics for this discharge was performed using the bounce averaged Fokker Planck code FPPRF[33] coupled to the full-wave electromagnetic field solver TORIC.[34] The coupled package is run within the transport analysis code

TRANSP.[35] Immediately following boronization in Alcator C-Mod, the background minority hydrogen concentration is estimated to be typically $n_H / (n_H + n_D) \approx 2\text{-}5\%$.[28] For the analyses shown in Figs. 5-6 this was assumed to be the case. Figure 5(a) shows the radial power absorption profiles predicted by TORIC for this discharge at 0.9 sec. About 71% of the power (2 MW) is absorbed via hydrogen minority heating, 20% of the power is absorbed at the deuterium second harmonic resonance, and 10% of the power is absorbed by electrons due to direct Landau damping of the incoming fast magnetosonic wave. The rather significant fraction of second harmonic heating is a consequence of the high plasma density and deuteron temperature that develops during the discharge. This leads to an increase in the background ion beta and consequently in the second harmonic heating. Plots of the left circularly polarized electric field in Fig. 5(b) demonstrate a unique aspect of the C-Mod ICRF heating experiments, namely that the high plasma density leads to significant focusing of the ICRF wavefronts near the magnetic axis. Figure 6(a) shows the power partition of the fast minority hydrogen tail at 0.9 sec. Again it is interesting to note that because of the high densities in C-Mod the fast ion tail couples only 58% of its power to electrons via drag, with the remaining tail power (42%) transferred via collisions to background deuterium. Strong coupling of tail power to the background deuterons provides a second source of ion heating in addition to the collisional exchange of power from thermal electrons to ions. A measure of the minority tail temperature [2/3<E>] is shown in Fig. 6(b), also corresponding to 0.9 sec. Here <E> is the energy moment over the quasilinear ion distribution function at each radius of the plasma. Consistent with the high plasma density, the minority tail temperatures are relatively low (< 60 keV) in this case.

The effect of hydrogen minority concentration on the total absorbed RF power efficiency $\eta_{abs} = P_{abs} / P_{inj}$ has also been investigated in C-Mod.[36] The concentration of hydrogen was varied and the heating efficiency was determined by analyzing the break in slope in the stored energy associated with an RF transition. The results from this type of scan are shown in Fig. 7. Here the stored plasma energy was calculated from EFIT[37] and the relative H concentration was measured using passive charge exchange. The heating efficiency peaks at about 85-90% for 10% H concentration. The high efficiency is not

surprising since single pass damping of the ICRF waves at the fundamental H-resonance in a deuterium majority plasma is expected to be high[30], as discussed above. As the minority fraction is increased above 10%, the heating efficiency saturates as the minority tail becomes less energetic and the wave absorption mechanism starts to make a transition over to mode conversion.

B. Fundamental ^{3}He minority heating

The fundamental minority ^{3}He heating scheme has also been tested on C-Mod in discharges at 7.9 T, 0.8 – 1.2 MA, using the D- and E- port antennas powered at 78 and 80 MHz. This scheme is of particular relevance for burning plasmas such as ITER where ^{3}He minority heating may be operative. Testing this scenario on C-Mod is somewhat challenging because in the case of an isolated fundamental resonance (^{3}He) in a deuterium majority plasma, the single pass damping is reduced significantly by a factor of $(E_+ / E_y)^2 = 1/9$, relative to the D(H) minority scheme.[30] An example[28] of D(^{3}He) minority heating in C-Mod is shown in Fig. 8. Here an ELM-free H-mode was obtained with 2.4 MW of ICRF power at a plasma current of 1.2 MA. An extended period of dithering occurred prior to transition to the ELM-free phase as seen in the D_α trace in Fig. 8. If the ICRF power is assumed to be fully absorbed then the energy confinement time during the ELM – free phase of this discharge corresponds to an H-factor of 1.5, relative to the ITER-89 scaling. In general it was found that machine wall boronization improved the performance in low single pass absorption regimes via a reduction in the radiated power. Overall heating efficiency was also investigated for the D(^{3}He) scheme by scanning the (^{3}He) concentration and again computing the heating efficiency from a break in slope analysis of the stored energy at a transition in the RF power. Results are shown in Fig. 9 and indicate a broad maximum of 70-75% in the heating efficiency extending from about 5-10% (^{3}He) concentration. The lower maximum heating efficiency relative to D(H) is perhaps a consequence of lower single pass damping allowing competition from edge ^{11}B and D fundamental absorption. Also, the drop-off in heating efficiency above 10% will be shown in Sec. IV to be due to a transition to the mode conversion regime due to the deposition profile moving off-axis. Future

experiments are planned on C-Mod to more directly compare the heating efficiency of the D(H) and D(^{3}He) minority heating schemes by carrying out experiments at the same magnetic field (5.3T), using two separate source frequencies, 50 MHz for D(^{3}He) and 80 MHz for D(H).

C. Physics performance of the four strap antenna

Despite the need for extensive iterative refinements in the design and fabrication of the four strap ICRF J-antenna that were discussed in Sec. II, the final physics performance of the antenna has been a great success. The heating efficiency and impurity production of the J-antenna have been found to be comparable to the two strap D- and E- antennas, when operated under a variety of conditions. Hydrogen minority heating was used in C-Mod to assess the performance of the 4-strap J-antenna. The results of one such study are shown in Fig. 10 for a discharge at 5.2 T and 0.8 MA. The D-, E-, and J- antennas were independently powered at the 1.25 MW level, each for about 200 msec. The D- and E- antennas were phased (0, π), producing balanced vacuum power spectra peaked at toroidal mode numbers of $n_\phi = \pm 10$. The J-antenna was operated in its so-called "heating" phasing (0, π, π, 0), which also produced a bi-directional vacuum spectrum peaked at $n_\phi = \pm 10$. In each case the increase in stored energy, central electron temperature, neutron rate, and impurity production was almost identical, indicating that the heating efficiency of the four-strap antenna is comparable to that of the two-strap antennas [see Fig. 10]. In each case the discharge remained in L-mode because the RF power remained below the H-mode power threshold.

Since the phasing of the J-antenna is variable, it can also be used to produce spectra for current drive ($\pm 90°$), where $\pm 90°$ correspond to relative strap phasings of (0,$\pm\pi/2$,$\pm\pi$,$\pm 3\pi/2$), and $n_\phi = \pm 7$. In order to compare the J-antenna performance under current drive phasing with heating phasing, a series of identical L-mode target plasmas were produced and ICRF power at three different phasings was injected into each discharge at the 2.8 MW level [see Fig. 11]. The change in stored energy, central electron temperature, electron density, and D_α was almost the same in each case,

indicating that the four-strap antenna was heating the plasma with about the same efficiency at each phasing. The comparable heating efficiency obtained for the different antenna phasings is somewhat surprising since the peaks in the vacuum power spectrum vary from $n_\phi = \pm 7$ to $n_\phi = \pm 10$, and the coupled power spectrum for the $n_\phi = \pm 10$ may be less efficient than for $n_\phi = \pm 7$. We note that variations in the poloidal mode spectrum due to toroidicity tend to broaden the injected power spectra in parallel wavenumber space, leading to more similarity in the wave propagation and absorption. Even more significant perhaps is the result that the impurity radiation did not increase any more with current drive phasing than it did with heating phasing. The most noticeable difference in Fig. 11 is the sawtooth period, which is longer for +90° than for −90°. This is an important example of sawtooth modification with ICRH that will be discussed further in Sec. IV(d).

D. Second harmonic minority heating experiments

The wide operating range in toroidal magnetic field and plasma current in C-Mod has made it possible to investigate second harmonic ion cyclotron heating experiments in minority hydrogen and (^{3}He) plasmas.[38] Since the second harmonic absorption is down by a factor of the background plasma ion beta (β_D) as compared to (n_H / n_D),[30] these heating schemes are characterized by low single pass absorption. In both the $2\Omega_H$ and $2\Omega_{He-3}$ experiments it was necessary to boronize the machine walls in order to obtain H-modes during the ICRF heating. With $2\Omega_{He-3}$, the best heating results were obtained in target plasmas at 4.2T, I_p=0.6 MA, and $n_e \approx 0.8 - 1.0 \times 10^{20}$ m^{-3}. The stored energy would increase from 0.025 MJ to 0.045 MJ with 2.2 MW of ICRF power. However, the confinement enhancement factor $H_{ITER-89}$ would remain close to unity, presumably being limited by impurity radiation and/or weak single pass absorption. Somewhat better results have been obtained with $2\Omega_H$ heating at 2.6 T, I_p=0.55 MA, and $n_e \approx 0.5 - 1.2 \times 10^{20}$ m^{-3}. The stored energy in H-mode would typically double from about 0.02 MJ to 0.035 MJ with $1.3 - 1.4$ MW of ICRF power. Confinement in these discharges was typically higher than in $2\Omega_{He-3}$, with $H_{ITER-89} \approx 1.4$. This was probably due to the higher single pass absorption expected in the hydrogen minority heating scenarios.

IV. ICRF MODE CONVERSION IN D(^{3}HE) AND D(H)

A. Observation of mode conversion electron heating in D(^{3}He) plasmas

During the past five years the ICRF physics research program on Alcator C-Mod has concentrated on the measurement of mode converted ICRF waves[39,40,41,42,43] and their use for plasma control. In parallel with this activity an extensive computational effort[44,45] was undertaken to simulate and interpret measurements made in these experiments and establish a predictive capability for the future use of mode converted waves in plasma control applications.

The earliest experiments with mode converted ICRF waves were carried out in D(^{3}He) discharges at 7.9 T using the D- and E- antennas driven at 80 MHz.[39,46] Direct electron heating by mode converted waves was deduced by modulating the ICRF power and performing a break in slope analysis of the electron temperature versus time as measured by the nine channel grating polychromator system (GPC).[32] An example of off-axis mode conversion electron heating (MCEH) observed with this method is shown in Fig. 12. The parameters for this discharge were $B_0 = 7.9$T, I_p=1.2 MA, $n_e(0) \approx 2.5 \times 10^{20}$ m^{-3}, $n_{He-3} / n_e \cong 0.24$, $n_H / n_e \cong 0.05$, and $n_D / n_e \cong 0.47$. The ^{3}He concentration was estimated from the density rise due to ^{3}He gas puffing, spectroscopic measurements of the HEII Ly$_\alpha$ line, and Z_{eff}. Evidence of the localized electron heating from the mode converted waves can be seen at the RF power transition where there is a clear change in the slope of the GPC channel at r/a = 0.6 [Fig. 12(a)]. In contrast, the central GPC channel shows far less change. Computing the local power density from the change in slope of the electron temperature versus time for all of the GPC channels yields the electron heating profile in Fig. 12(b).

A study of the electron heating versus ^{3}He concentration is summarized in Fig. 13.[44,45] The percentage of incident power going into direct MCEH was observed to increase dramatically as the relative concentration of ^{3}He was increased above 10%, signaling the

transition from minority heating to IBW mode conversion. A toroidal full-wave ICRF code (TORIC)[34,44,45] was used to simulate this mode conversion process. The code uses an ion conductivity operator valid in the finite ion Larmor radius (FLR) regime, where $[(k_\perp \rho_i)^2 < 1]$. The conductivity operator was also modified[47] to yield the correct electron Landau damping of the mode converted ion Bernstein (IBW) and ion cyclotron (ICW) wave at arbitrary $k_\perp \rho_i$. The code employs a spectral Ansatz for the electric field of the form:

$$\vec{E} = \sum_{n_\phi} \sum_m \hat{E}_m(\rho) \exp(im\theta + in_\phi\phi),$$

where (m, n_ϕ) are the poloidal and toroidal mode numbers, and ρ is the square root of normalized toroidal flux, approximately equal to (r/a). The number of poloidal modes retained in the spectral expansion is denoted by N_m. Typically N_m in the range of 63 modes with $-31 \leq m \leq +31$ is sufficient to resolve the fast magnetosonic mode. However, numerical resolution of the mode converted IBW requires m-numbers that satisfy $k_\perp \rho_i \approx 1$, where $k_\perp \approx (m / r_{MC})$. For D(^{3}He) mode conversion in C-Mod at $B_0 = 8$T, $T_i \approx 2$ keV, and $n_{He-3} / n_e \cong 0.25$, we obtain $\rho_D \approx 0.08$ cm, $r_{MC} \approx 10$ cm, $m_{max} \approx 125$, and $N_m \approx 250$.[44] In order to obtain full-wave solutions of mode converted waves with 255 – 1000 poloidal modes, a parallel, out of core matrix inversion algorithm was implemented[45] in TORIC and the calculations were carried out on the MARSHALL parallel computing cluster at MIT. The need for adequate numerical resolution in the full-wave solver is clearly seen in Fig. 13 where TORIC predictions for mode conversion electron heating were superposed on the experimental data. Simulations done with only 15 poloidal modes grossly underestimate the fraction of mode converted power damped on electrons as n_{He-3} / n_e is increased above 15-18%. In contrast, the simulations performed with 255 poloidal modes are in much better agreement with experiment. Figure 14 displays the wave electric fields from a TORIC simulation in Fig. 13, corresponding to $n_{He-3} / n_e = 0.24$, $N_m = 255$, and $N_r = 480$ radial elements. The fast wave electric field can be seen on the tokamak low field side (LFS) where $X \equiv (R - R_0) > 0$. Mode converted IBW wave fields are evident as vertical plane wave fronts on the high field side (HFS) where $X \equiv (R - R_0) < 0$. When inadequate mode resolution is used in the

simulations, the plane wave fronts on the HFS tend to "bend" back towards the LFS, intersecting the ^{3}He resonance chord passing through the axis, resulting in spurious ^{3}He ion cyclotron damping off-axis.[44] Thus in order to even qualitatively reproduce the measured electron damping of mode converted IBW in C-Mod, a significant computational development program was necessary.

B. Detection and simulation of mode converted ICRF waves in C-Mod

The actual detection of mode converted ICRF waves became possible on Alcator C-Mod with the installation of a phase contrast imaging (PCI) diagnostic.[48,49,50,51] This diagnostic technique makes it possible to observe a large region of the plasma cross-section and a wide range of wavenumbers simultaneously. However, spatial localization is limited since the diagnostic laser path is chordal. The C-Mod PCI system uses a 10.6μm wavelength CO_2 laser, expanded to a spatial width of 15 cm, and passing through the central portion of the plasma, as shown in Fig. 15.[50,51] Mode converted ICRF waves drive strong electron density fluctuations that can scatter the CO_2 laser beam. The interference of this scattered light with appropriately phase shifted unscattered radiation passing through the plasma can then be detected. This technique is ideal for detecting mode converted ICRF waves since the diagnostic is most sensitive to perturbations whose surfaces of constant phase are aligned vertically with the laser beam, such as the mode converted wavefields shown in Fig. 14.[40] Although perturbed electron density fluctuations from the wavefields occur at about 80 MHz, the laser intensity is modulated at a frequency that is offset from the driving frequency by about 0.3 MHz. The 80 MHz fluctuation in the plasma is therefore illuminated by the 80.3 MHz modulated laser and the image intensity which is the product of both signals exhibits a 300 kHz beat oscillation. This is the frequency at which the signal is detected. Finally, the raw PCI data is Fourier transformed in time and space, resulting in data converted to frequency and wavenumber.

An example[40] of this detection technique is shown in Fig. 16(a) for mode conversion in a three species plasma in C-Mod at B_0 = 5.84T, I_p = 800 kA, 59% H, 4% ^{3}He, 33%D, $n_e(0)$

= 2 × 10^{20} m^{-3}, and T$_e$(0) = 1.3 keV. Two extremely interesting features of this measurement are first, that the phase velocity of the detected wave is positive, corresponding to propagation toward the LFS of the H-(^{3}He) hybrid resonance and second, the detected wavenumber (≈ 7-8 cm^{-1}) is intermediate to the incident fast wave and the ion Bernstein wave. Careful analysis of the local dispersion [see Fig. 16(b)] for this case reveals the excitation of a third mode of propagation, namely the mode converted ion cyclotron wave (ICW).[40,41] As clearly seen from the local dispersion relation, the mode propagates to the LFS of the ion-ion hybrid layer and is characterized by wavelengths in the range of (5 cm^1 ≤ k$_\perp$ ≤ 10 cm^{-1}), in substantial agreement with the detected wavelengths. The ICW was first predicted to exist by Perkins[52] for mode conversion in a D-T fusion plasma. In that work it was pointed out that a critical element for the wave to exist is the presence of a local poloidal field.[52] For the dispersion relation shown in Fig. 16(b), mode numbers of n$_\phi$ = 13 and m=0 were used and the ICW wave root was solved along a flux surface where B$_\theta$ = 0.25T.

An example of the detected scattered wave spectrum is shown in Fig. 17 where the line integrated PCI signal is plotted versus major radial position (R).[40] The plasma parameters in this case were B$_0$ = 5.84T, I$_p$ = 1 MA, 50% H, 8% ^{3}He, 34% D, n$_e$(0) = 2.5 × 10^{20} m^{-3}, and T$_e$(0) = 1.3 keV. Short wavelength structures can be seen to the LFS of the ion-ion hybrid layer with a separation between amplitude peaks of about 1 − 2 cm. This wavelength corresponds to the ICW as it is longer wavelength than the IBW (typically a few mm) and shorter than the fast wave wavelength of about 5 cm. The presence of the mode converted ICW was also confirmed through massively parallel simulations using both the TORIC full-wave solver[40,45] and the all-orders spectral solver AORSA.[53] An example of an ICW simulation using the TORIC solver is shown in Fig. 18 and reveals the complex topology of this mode conversion process in the 2D tokamak geometry. Plasma parameters used in this simulation were typical of the discharges in Figs. 16(a,b) with 21% D, 23% ^{3}He, and 33% H. A toroidal mode number of n$_\phi$ = 13 was used with 240 radial elements, 255 poloidal modes, and contours of the Re(E$_{//}$) have been plotted. In addition to the ICW wavefields on the LFS of the ion-ion hybrid layer, the simulation also reveals the presence of mode converted IBW near the midplane on the

high field side. The measurements in Fig. 16(a) and Fig. 17 do not show the presence of the IBW because the density fluctuations associated with the IBW are much lower amplitude than those driven by the ICW.[40] Also, the power mode converted into the IBW branch is found to be quite low in these simulations. An outstanding feature of the full-wave simulation in Fig. 18 is the up-down asymmetry in the ICW wave fields. This is a consequence of the large poloidal mode numbers associated with the mode converted waves (typically $|m| \geq 50 - 80$) and the presence of the poloidal magnetic field. Ion cyclotron waves below the midplane undergo an increase in $k_{//}$ and damp rather quickly due to electron Landau damping, whereas ICW above the midplane experience a downshift in their ($k_{//}$) and propagate farther before damping. Since $k_{//} = [(m/r)B_{\theta}/B + (n_{\phi}/R)B_{\phi}/B)]$ and m is quite large in these simulations, the poloidal field converts variations in the m-spectrum into large changes in $k_{//}$.

C. Synthetic PCI diagnostic for mode converted ICRF waves

Combined application of the PCI diagnostic for ICRF wave detection and advanced ICRF full-wave solvers for simulation has resulted in a pioneering level of understanding between theory and experiment in the area of wave-particle interactions. In order to take advantage of ICRF mode conversion processes for localized current generation and pressure profile control, a synthetic PCI diagnostic was also developed[40,42,43] and is now routinely used on Alcator C-Mod. The line integrated PCI signal shown in Fig. 17 can be simulated using the simulated ICRF electric and magnetic fields from the TORIC solver to compute the fluctuating electron density n_{el} associated with the mode converted waves[40,43]

$$n_{e1} \approx \frac{-i}{\omega} n_{e0} \nabla \cdot \vec{v}_{e1},$$

$$v_{e1,//} \approx \frac{-i\omega_{ce}}{\omega} \frac{E_{//}^{rf}}{B^{rf}},$$

$$v_{e1,\perp} \approx \frac{E_{\perp}^{rf}}{B^{rf}}.$$

The total fluctuating electron density at the spatial location of the PCI is obtained by summing n_{e1} contributions from all toroidal modes in the antenna power spectrum at that point. The contribution from each mode is weighted by the partial loading resistance for that mode, taking into account the vacuum power spectrum of the antenna. An example of the predicted fluctuating electron density contours for an off-axis ICRF mode conversion experiment in C-Mod is shown in Figs. 19(a,b).[43] This simulation corresponds to a discharge with B_0 = 5.57T, I_p = 1 MA, 5% H, 11% ^{3}He, 85%D, $n_e(0)$ = 2 $\times$ 10^{20} m^{-3}, and $T_e(0)$ = $T_i(0)$ = 2.1 keV. The four strap J - antenna was used in this experiment with the tunable ICRF sources set at 50 MHz. A toroidal mode number of n_ϕ = 7 was taken, corresponding to the peak power lobe in the vacuum spectrum. The concentration of ^{3}He was determined from a series of TORIC simulations in which the ^{3}He level was varied until the electron heating profile in the code agreed with the electron heating as determined from a break in slope analysis of the electron temperature versus time, at a fast RF shut-off. A concentration of 11% gave the best agreement with experiment as can be seen in Fig. 19(c). In this case the TORIC prediction for electron absorption via the mode converted waves was 37% of the injected power compared to the experimentally determined electron absorption which was 38% ± 8%. The T_e profile in these experiments was measured using a high spatial and temporal resolution electron cyclotron emission (ECE) system.[54] Finally, the comparison between the synthetic and measured PCI signals is shown in Fig. 20. Good agreement is seen in the shapes of the real and imaginary parts, although the magnitudes have been scaled. Short wavelength structures are evident on both the low field and high field side of the ion-ion hybrid layer, suggesting that both IBW and ICW were simultaneously observed. Investigation of the up-down asymmetry in the ICW fields is difficult owing to the line-integrated nature of

the PCI signal. However, double humped PCI distributions have been seen both experimentally and with the synthetic diagnostic for cases involving on-axis mode conversion.[43]

D. Observations of mode conversion electron heating in D(H) plasmas

In addition to mode conversion electron heating in plasmas with D(^{3}He) and H(^{3}He) ion compositions, electron heating by mode converted waves has also been observed in D(H) plasmas with high H-concentration (typically $\approx$ 20%).[55] Electron heating by mode converted waves was inferred in these experiments by a break in slope technique applied at the RF turn-off transition. The electron temperature was measured using the high resolution 32 channel ECE system.[54] The hydrogen fraction was inferred from the Balmer - α line ratio of D and H neutrals at the plasma edge[56] and a constant radial profile for the hydrogen fraction was assumed. An example of near on-axis mode conversion electron heating in C-Mod is shown in Fig. 21(a) along with the predicted electron heating profiles from the TORIC full-wave solver.[55] The RF frequency in this case was 70 MHz and the RF power was coupled using the J-antenna. The discharges were produced with B_0 = 5.27 T, 19% H, 81% D, I_p = 1MA, n_e = 1.7 $\times$ 10^{20} m-^{3}, and T_e = 1.5 – 2.5 keV. In these cases the ion-ion hybrid layer was close to the plasma center while the H-cyclotron resonance layer was located at about r/a=0.36 to the LFS. The experimentally deduced electron heating profile is fairly narrow and the integrated RF power fraction to electrons is 0.16, integrated out to r/a = 0.25. Deposition profiles from TORIC were constructed by summing and weighting the contributions from 20 toroidal modes in the antenna spectrum. The magnitude and shape of the predicted electron heating is remarkably close to the experimental result and the integrated RF power to electrons (0.16) is also close to the experimental value. TORIC modeling indicates the remaining power is absorbed via ion cyclotron damping in a broad region around the H-resonance layer (0.2 < r/a < 0.5). The shaded area in Fig. 21(a) indicates the "noise floor" associated with the break in slope method. Contours of RF power absorption to electrons are shown in Fig. 21(b) for the central toroidal mode number in the antenna power spectrum (n_ϕ = 13). Planar type contours of heating to the HFS of the mode conversion layer suggest that the electron damping is primarily due to mode converted IBW. This is consistent with the notion that B_θ is small near the axis and thus the ICW cannot be excited near that point.[55]

Off-axis MCEH was also observed in C-Mod using the E-antenna driven at 80 MHz. An example of the inferred electron heating by mode converted waves is shown in Fig. 22(a). Again for comparison the predicted heating from TORIC is shown. The hydrogen concentration in this discharge was 22% H with 78% D. In this case the H-resonance was near the plasma center and the ion-ion hybrid layer was located off-axis on the HFS at r/a=0.4. Again both the magnitude and shape of the experimental and predicted heating profiles agree quite well. The integrated RF power fraction to electrons from the experiment is 0.20, as compared to the predicted integrated power fraction of 0.18 from TORIC. Two-dimensional contours of the electron absorption have been plotted in Fig. 22(b) for the peak power mode in the antenna spectrum, $n_\phi = 13$. There is now evidence of electron damping on both the low field and high field side of the ion-ion hybrid layer. Presumably mode converted IBW were responsible for the electron heating on the HFS and mode converted ICW were damped on the LFS. This picture is also consistent with the mode conversion layer being located off-axis where there is a finite poloidal field that is needed for excitation of the ICW.[52,55]

E. Sawtooth modification experiments using mode conversion current drive and minority heating

It is known that the sawtooth behavior can be modified, that is the period can be lengthened (stabilizing) or shortened (de-stabilizing) by respectively decreasing or increasing the current gradient at the q=1 surface.[57,58] Mode conversion current drive (MCCD) is ideally suited for this purpose since the electron deposition layer is relatively narrow. Sawtooth modification experiments[59] were carried out on Alcator C-Mod using mode converted ICRF waves to generate localized current near the q=1 surface. Deuterium plasmas were produced at 8T, Ip=0.8 MA, and the ^{3}He concentration was scanned to maximize the electron deposition slightly off-axis, near the q=1 surface. The J-antenna provided 1.5 MW of MCCD power at 78 MHz, and was operated in the co-current (CD) (+90°) and counter-CD (-90°) phasing. The D-antenna provided about 1.0 MW of power at 80 MHz and was operated in the heating phasing (0,π). As shown in Fig. 23(a), the sawtooth period increases from 10 msec to about 15 msec for counter-CD

phasing and shortens to about 5 msec for co-CD phasing. The measured electron power deposition profiles shown in Fig. 23(b) indicate the deposition profiles for co- and counter- CD phasing are similar with both peaking just inside the q=1 surface. The likely difference in these cases is the direction of MCCD, where counter-CD phasing would be expected to locally reduce the total current density at the deposition location, reducing the magnetic shear at that point and thus stabilizing the sawteeth. Conversely, co-CD phasing would increase the current density near the deposition layer, resulting in an increase in the magnetic shear at that point, thus de-stabilizing the sawteeth. Further experiments were performed to confirm the importance of the current drive location. The discharge shown in Fig. 23(a) with counter-CD phasing and local power deposition near the q=1 surface was repeated with the deposition layer moved to near the axis. In this case the sawtooth period was not modified, consistent with no longer having a local shear reduction at the q=1 surface. In the future, experiments will also be carried out where discharges will be created with co-CD phasing and power deposition outside of the q=1 surface. This should also produce a loss of local shear reduction near the q=1 surface, resulting in a loss of sawtooth stabilization.

In the discharges shown in Fig. 23(a), the fraction of power flowing into mode converted waves was estimated to be about 30%. The driven current that can be expected in this case was computed[60] using the local electron heating rate due to the mode converted waves as predicted by the TORIC solver. An estimate of the current drive efficiency may then be obtained from an adjoint treatment of the Fokker Planck equation:[61]

$$J_{rf}^{n_\phi}(\rho) = \int_0^{2\pi} d\theta \sum_m G_{rf}(\rho,\theta,v_{//}^m = \omega/k_{//}^m) \sum_{m'} \cdot S_{rf}^{ELD}(\rho,\theta,m,m').$$

Here $G_{rf}(\rho, \theta, m)$ is the parameterized current drive efficiency from Ehst-Karney and S_{rf} is computed by TORIC. TORIC simulations using this method indicate that only about 10 kA of current is expected to be generated in this case. Thus the MCCD cannot be detected through changes in the loop voltage as done in previous experiments on TFTR.[62,63] On the other hand, simulations of the MCCD' also indicate the local current

density from MCCD can be comparable to, or higher than the ohmic current density near the axis. Thus significant modification of the local current density can be expected in these experiments from the MCCD.

Energetic particle modification of sawteeth during hydrogen minority heating has also been observed in Alcator C-Mod. In fact an example of this was already shown in Fig. 11 where the heating efficiency of the four strap J-antenna was compared for current drive phasing ($\pm 90^0$) and the heating phasing. An enlargement of the central electron temperature trace (0.86 – 0.94 sec) is shown for this case in Fig. 24. The magnetic field is 5.2 T, the relative H concentration is less than 5%, the antenna was powered at 80 MHz, and therefore only minority heating was possible. The sawtooth period is seen to be 15 msec with $+90^0$ phasing, about 5 msec with -90^0 phasing, and 8-15 msec. with heating phasing. From these observations, it can be inferred that the sawtooth period was being modified by energetic particle production associated with the minority hydrogen tail. Modeling studies carried out with TRANSP / FPPRF for discharges at similar line averaged densities ($\leq 1 \times 10^{20}$ m^{-3}) indicate minority tail temperatures can exceed 300 keV in C-Mod[64] inder these conditions. An understanding of the dependence of the sawtooth behavior on antenna phasing will require more detailed modeling studies however.

V. CURRENT PROFILE CONTROL STUDIES IN THE LHRF IN ALCATOR C-MOD

A. Physics basis for Advanced Tokamak Operation in Alcator C-Mod using Lower Hybrid Current Profile Control.

The vision of an attractive tokamak reactor has improved dramatically over the last decade, largely due to the possibility of high-performance steady-state tokamak operating regimes, i.e., regimes with good confinement sustained by current that is largely driven by the bootstrap effect. While there are experimental indications that such regimes can indeed be achieved, high-performance, high-bootstrap-fraction regimes with fully non-inductive current drive have not yet been produced for pulse durations significantly greater than the resistive diffusion time. Thus the realization of attractive tokamak reactor regimes remains uncertain and dedicated experiments are required to verify the assumptions used in advanced reactor designs. A central objective of the lower hybrid current drive (LHCD) experiments planned for Alcator C-Mod is to supplement the bootstrap current with lower hybrid current drive in order to develop attractive steady-state regimes, namely those with high bootstrap fraction ($\geq$ 70%), high β_n ($\sim$ 3) and good confinement ($H_{\text{ITER-89}} \sim 2.5$).[65,66] If successful, these experiments will help to support the design basis for advanced tokamak reactor designs,[67] at least up to moderate bootstrap fractions ($\sim$70%), as well as to provide a basis for advanced regime operation in ITER. In addition to providing access to AT regimes, the off-axis LHCD capability will also be used to investigate sawtooth stabilization and suppression of neo-classical tearing modes (NTM's).

Alcator C-Mod is particularly well suited for the development of these so-called AT scenarios. The internal PF coils enable the strong shaping required for high β_n operation and the installed ICRF system is capable of sufficient ICRH source power (8 MW) to reach high β_n at $\sim$5 T field. Because of the unique capability of the cryogenically cooled magnets, discharges can be sustained at a field of 5 T for pulse durations up to 5 s, a time that corresponds to several resistive diffusion times. Lower hybrid current drive is also a good fit to AT research in Alcator C-Mod since it has proven current drive capability[68]

with the highest efficiency, typically $\sim$ 0.2 MA/MW-m^2, and is especially compatible with small, compact tokamak designs such as Alcator C-Mod. Furthermore, lower hybrid waves can be used to drive current efficiently in the outer half of the tokamak cross-section, consistent with the requirements of a flat or reversed shear profile and a broad pressure profile.

B. Simulations of advanced tokamak regimes for Alcator C-Mod

Early scoping studies' of viable AT operating modes in Alcator C-Mod employed the ACCOME current drive and MHD equilibrium solver[69] coupled to the PEST-II[70,71] ideal MHD stability code. The ACCOME code computes driven currents due to neutral beam injection (NBI), directed lower hybrid waves, injected ICRF waves, and bootstrap effects. These currents are used to compute a new MHD equilibrium by solving the Grad Shafranov equation. The MHD solver and current drive modules are iterated until a self-consistent solution is obtained. The MHD solution is then tested for stability to the n=∞ ideal ballooning mode as well as the low n=(1,2,3) external kink modes. These studies employed model profiles for the density and temperature having the forms,

$$p(\psi) = p(0)(1-\psi)^2,$$
$$T(\psi) = T(0)[\tfrac{2}{3}(1-\psi)^{7/2} + \tfrac{1}{3}(1-\psi^8)^{3/2}],$$
$$n(\psi) = p(\psi)/T(\psi),$$

where ψ is the normalized poloidal flux (0$\leq \psi \leq$ 1). The central density and temperatures were taken to be $n_e(0)$ = 2 $\times$ 10^{20} m^{-3}, and $T_e(0)$ = $T_i(0)$ = 7.5 keV, based on a confinement enhancement factor H=2.5, relative to the ITER-89 scaling, and assuming 4 MW of available ICRF heating power and 3 MW of LHRF power. The magnetic field was 4.0T and the current was 0.8 MA. The LH source frequency was 4.6GHz and the central parallel refractive index ($n_{//}$) of the LH waves was taken to be 3.0. The predicted current densities and safety factor profiles are shown in Fig. 25. The total plasma current in Fig. 25(a) is I_p = 0.81 MA with a bootstrap fraction f_{BS} = 0.74, total LH current of I_{LH} = 0.196 MA, and a central fast wave seed current of 9 kA. The profile of safety factor is clearly shear reversed with q(0) = 3.95, q(min) = 2.65, and q(95) = 6.35. The normalized

plasma beta is β_N = 2.96 (%-m-T/MA) and the pressure peaking factor is p(0) / p_{avg} =2.90. This plasma is also highly shaped with elongation κ_χ = 1.77 and triangularity δ_χ = 0.71 [see Fig. 26].

Ideal stability properties of the equilibrium in Fig. 25 were studied in detail using the JSOLVER-PEST-II MHD/stability codes.[65]   A parametric scan was performed in pressure ($\varepsilon\beta_p$) and current (q_*) using the ACCOME equilibrium as a reference discharge. First at fixed current, the ideal stability was tested for equilibrium solutions that were scaled in pressure from the ACCOME reference case.   Then at fixed pressure, ideal stability was tested for equilibria that had been scaled in current. The resulting stability diagram is shown in Fig. 27 as boundaries of stable equilibria in an $\varepsilon\beta_p$ versus q_* space. The dotted lines correspond to lines of constant normalized beta while the dark blue, red, and green curves correspond to stability boundaries set by the n=∞, n=1, and the n=2 ideal modes, respectively, without a conducting shell. The n=1 external kink mode is the lowest boundary and therefore sets the overall stability limit for the reference equilibrium. Shown also in light green is the stability boundary with a conducting shell placed at 1.3a. Clearly the ideal β-limit is significantly higher when the conducting shell is present. It has been found in several studies[65,72] that high elongation and especially high triangularity are beneficial for increasing the no-wall ideal β-limit and these results are suggestive of this fact. For example, the reference case produced with ACCOME was found to be stable up to a β_N of about 3.2 without a conducting shell [see Fig. 27]. If the triangularity is reduced to zero or the elongation is set to 1.0 then the ideal β-limit is found to drop to about 2.0 or less.[65]

C. Lower Hybrid Current Drive Studies in Optimal Target Discharges

In the high quality H-modes typically produced in Alcator C-Mod, the pedestal and average densities tend to be rather high e.g., 2-3 × 10^{20} m^{-3} and 3-4 × 10^{20} m^{-3} respectively. Modeling of the effect of LH current drive for these discharges shows that the driven current fraction would be low and would tend to be localized near the edge.

Therefore we have undertaken a campaign aimed at producing H-Mode discharges with lower density and higher temperature that are more suitable for injecting LHCD. This was found to be possible, mainly by lowering the initial L-Mode target density and plasma current, and a number of discharges suitable for LHCD injection have been obtained. Density and temperature profiles from a typical case are shown in Fig. 28. The discharge shown in Fig. 28 was obtained using 3.4 MW of ICRF power for hydrogen minority heating at $B_0 = 5.4T$ and $I_p = 0.6$ MA.

The effect of applying 3 MW of lower hybrid power to these discharges was recently examined using the CQL3D – GENRAY suite of codes.[73,74] Magnetic parameters (shape, current and field), plasma profiles, and MHD equilibrium were taken from the experimental data for these simulations. The CQL3D code computes a time dependent solution of the 2-D velocity space Fokker Planck equation with radial diffusion as an option that was turned off in these simulations. The GENRAY code solves the ray equations in toroidal geometry using the numerical equilibrium from an EFIT reconstruction of the plasma discharge. The assumption of neglecting radial diffusion of fast electrons in CQL3D is justified in the case of C-Mod because the fast electron energies are expected to be on the order of 100 keV ($n_{//} \approx 2$) and the plasma densities above 1.0×10^{20} m^{-3}. In this case the slowing down time of the fast electrons is short (3 – 5 $\times$ 10^{-3} sec) compared to a typical spatial diffusion time scale (0.01 – 0.02 sec for example). Thus fast electrons would be expected to thermalize before they diffuse any appreciable distance in C-Mod. A LH power spectrum corresponding to relative waveguide phasing of 90 degrees was chosen with 2.0 MW of injected power. Lower hybrid power in the co-CD direction was characterized by $n_{//}(0) = 2.33$, and LH power in the counter-CD direction was characterized by $n_{//}(0) = 7.5$. The LHRF deposition and current density profiles computed with CQL3D and GENRAY are shown in Fig. 29. The total integrated LH current is 185 kA. Approximately 0.5 – 0.6 MW is absorbed in the plasma core with about 0.6 MW absorbed in a narrow deposition layer peaked off-axis at r/a = 0.75. Lower hybrid power damped at $0.9 \leq \rho \leq 1$ in Fig. 29(a) corresponds to the counter launched power at high $n_{//} = 7.5$, as well as some forward power that is not damped on the first pass into the plasma. . In Fig. 29(b) it can be seen that this power is

responsible for a small counter – CD at the plasma edge. Using an average electron density of 1.3×10^{20} m^{-3}, $I_{LH} = 0.185$ MA, $R_0 = 0.67$ m, and $P_{LH} = 2$ MW, the current drive figure of merit in this case is found to be $\eta_{CD} = (n_e\, I_{LH}\, R_0\, /\, P_{LH}) = 0.081$ (10^{20} A/W/m^2). This figure of merit is quite acceptable considering the relatively high value of parallel refractive index of the forward power ($n_{//} = 2.33$) that is needed to both insure wave absorption outside the plasma core and satisfy LH wave accessibility ($n_{//} \geq n_{//acc}$). Note that at $\rho = 0.65$, $B_0 \approx 4.5$ T, $n_e(\rho = 0.65) \approx 1.5 \times 10^{20}$ m^{-3}, and $n_{//acc} = 2.1$, so that $n_{//}$ > 2.1 is needed as a minimum to guarantee wave accessibility at $\rho \geq 0.5$. Furthermore, this current drive figure of merit is consistent with past LH current drive experiments on Alcator C[68] at lower density [$n_e(0) \approx (0.3 - 1.0 \times 10^{20}$ m^{-3}] and higher magnetic field strength ($B_0 \approx 5 - 8$T). The lower density and higher magnetic field strength in those experiments resulted in improved wave accessibility, allowing higher phase velocity LH waves ($n_{//} \approx 1.3 - 1.5$) to be coupled to the plasma. This resulted in a correspondingly higher current drive figure of merit [$\eta_{CD} \approx 0.15 - 0.20$ (10^{20} A/W/m^2)].[68]

The physics requirements placed on the LH launcher design, namely to have a highly directional, narrow power spectrum, characterized by parallel refractive indices in the range $2 \leq n_{//} \leq 3$ was a technological challenge at 4.6 GHz because of the relatively narrow widths of the individual waveguides of the launcher. Details of this launcher design, fabrication, and initial results are discussed in the following section.

VI. THE ALCATOR C-MOD LOWER HYBRID EXPERIMENT

A. Introduction

A new lower hybrid current drive system has been implemented on Alcator C-Mod. The main components are an RF transmitter capable of delivering 3 MW of RF power at 4.6 GHz, and a launcher composed of 96 waveguides arranged in 4 rows of 24 waveguides. Each of the 12 klystrons drives 2 columns of waveguides with a relative phase determined by the setting of a high power phase shifter. The phases of the 12 klystrons are electronically controllable, which allows the applied $n_\parallel$ spectrum to be varied over the range $1.5 < n_\parallel < 3$ with a time response of less than 1 ms. Preliminary measurements of the coupling efficiency show that reflection coefficients as low as 6% are obtained by operating with density at the grill of 3×10^{18} m^{-3} and at the optimal current drive phasing of 90°.

The main tools for the LH current profile control experiments, summarized in Table 1, are the existing ICRF system, with a source power up to 8 MW, and a LH system operating at 4.6 GHz with an initial capability of 3 MW source power applied to a single grill. A second grill and an increase of the source power to 4 MW are planned for a second phase. Taking into account waveguide losses and power density limitations, the maximum delivered LH power is expected to be limited to about 2 MW during Phase I operation. At the lower power density afforded by two grills, the power delivered to the plasma in Phase II is expected to increase to 3 MW even though only one additional MW of source power will be added.

In Section B, we describe the main engineering details of the launcher. Section C provides an overview of the RF transmitter system. The grill spectral capability and preliminary coupling results are presented in Section D and a short summary follows in Section E.

B. Launcher Fabrication

A cross-sectional drawing of the LHCD launcher assembly mounted in an Alcator C-Mod port is shown in Fig. 30. Three subassemblies can be identified. Working back from the plasma they are the couplers, the forward waveguide assembly and the rear waveguide assembly. The RF power is coupled to the plasma by means of 96 waveguides arranged in 4 rows with 24 waveguides in each row. The vacuum windows are located in the coupler waveguides and are positioned well forward of the position of cyclotron resonance at the operating frequency of 4.6 GHz. Photographs of the four couplers as they appear facing the plasma are shown in Fig. 31. The launcher is fed by 12 klystrons, each capable of delivering 250 kW of CW power at 4.6 GHz. The power from each klystron is split 8 ways and delivered to 2 columns of waveguides as indicated schematically in Fig. 32. A single oscillator-amplifier provides the excitation to all klystrons. The output is divided 12 ways and fed to a vector modulator that provides independent in-phase and quadrature-phase (I/Q) control of the input drive to each klystron. A mechanical phase shifter can be used to vary the relative phase of the two columns of waveguides fed by the same klystron, but only between plasma shots. Nevertheless, a substantial range of $n_{//}$ control, e.g., $1.5 - 3$, is possible using only the electronic phase shifter.[75] Details of each subassembly are provided in the following subsections.

(i) Couplers

Each of the four couplers shown in Fig. 31 consists of 24 waveguides measuring 5.5 x 60 mm in cross-section. They were initially fabricated from blocks of titanium (Ti-6Al-2Sn-4Zr-2Mo) by wire electrical discharge machining (EDM). The thickness of the waveguide walls (and thus the septa between adjacent waveguides) is 1.5 mm. Ceramic (Al_2O_3) windows are brazed into each of the waveguides near the end of the coupler that joins to the forward waveguide assembly. A viton O-ring located between the couplers and the forward waveguide assembly flange forms the vacuum seal. Care was taken to ensure that proper pressure could be simultaneously applied to the O-ring (originally

designed to be a gold wire) and an aluminum gasket that forms the RF seal between the couplers and forward waveguide assembly.[76]

Brazing Al_2O_3 windows into metallic waveguides is challenging since the coefficients of thermal expansion (CTE's) are not well matched over the temperature range involved. Titanium was chosen for the coupler material since its CTE is closer to that of Al_2O_3 than that of most metals. While the two CTE's are nearly equal at room temperature, they diverge monotonically as the temperature is increased to typical brazing temperatures. In the case of the CuSil braze used, the measured integral of the difference between the CTE of Ti and that of Al_2O_3 increases to 0.24% as the temperature increases from 25 °C to the brazing temperature of ~ 800°C.

There are two consequences of the differential expansion that occurs during the brazing process. One is the difficulty in ensuring the correct room temperature gap and amount of braze so that surface tension will be sufficient to uniformly fill the gap between window and waveguide at the braze temperature, the other is that upon solidification and cooling to room temperature residual stresses are set up in the ceramic that can result in crack formation and propagation. In the case of the couplers it was found that a room temperature gap of ≤ 0.05 mm together with the use of two preformed braze wires of diameters 0.75 and 1 mm resulted in a high quality braze that required minimal cleanup after brazing.

The tensile stresses resulting from the differential contraction are particularly high in the outermost windows but were reduced to acceptable levels by 1) thinning the titanium waveguide wall thickness from 1.5 mm to 0.75 mm on the outer waveguide walls (i.e., the outer broad wall on waveguides 1 and 24) in the area of the windows, and 2) by brazing a thin ceramic section to the outer wall where it had been thinned (see Fig. 33). Adding the thin ceramic to the outer walls simulates having a window there to balance out the load on the outer wall. Balancing the load reduces the stress on the outboard windows, eliminating cracks.

Titanium reacts with hydrogen to form titanium hydride and the reaction can be particularly rapid at high temperature. To prevent the formation of the hydride in the machine, it was planned to plate the couplers with copper. However, initial attempts at plating were unsuccessful as it was found that the plating did not adhere to the titanium at elevated temperature. In order to gain operating experience with the system, the couplers were installed in Alcator C-Mod without plating. The hydride did indeed form, but more rapidly and extensively than had been expected. While sufficient for investigating the coupling efficiency at modest power (~ 200 kW), it was necessary to remove the coupler after only a few months in the machine. It is now planned to replace titanium with 304-L stainless steel. FEA analysis confirmed by R&D tests suggests that techniques can be developed to braze the windows even in spite of the disparate CTE's.

(ii) Forward Waveguide Assembly

The forward waveguide assembly (FWA) consists of 25 stainless steel plates with 4 waveguide channels milled into one side of 24 of the plates. When the plates are stacked and bolted together, the channels formed by the milled side of one plate pressed to the flat side of the adjacent plate form the waveguides feeding the couplers. The design follows that used in LH experiments on PBX-M, which had a stack of 33 plates forming 32 waveguides. Stainless steel series 304 was used for the plates since the use of higher conductivity materials such as copper or aluminum would have resulted in unsustainable disruption loads. However, since the microwave loss in stainless steel guides would have been significant over the 1.25 m length, the plates were copper plated before assembly. After polishing, the transmission loss in the waveguides in the stacked assembly was measured to be about 0.33 dB/m except for two waveguides that had an attenuation of 0.5 dB/m. An attenuation of 0.33 dB/m corresponds to ~3.5 times the theoretical loss calculated for copper waveguides with the same dimensions.

The FWA waveguides also include H-plane tapers that transform the 6 cm width of the coupler waveguides to the 4.75 cm width of standard WR 187 waveguides. Flexibility in the location of the H-plane tapers in the two top and two bottom adjacent guides is taken

advantage of to cancel differential phase shifts of 90° introduced by the 3 dB couplers in the rear waveguide assembly, as well as to compensate for unavoidable additional phase shift caused by the poloidal curvature of the couplers. In this way, poloidal phase variation over each set of 4 vertically aligned waveguides in the couplers can be minimized. A photo of the copper plated FWA is shown in Fig. 34.

(iii) Rear Waveguide Assembly and Splitter Network

The rear waveguide assembly (RWA) follows the design of the FWA, i.e., it is also fabricated from 25 stacked plates with 4 waveguide slots milled into one side of 24 of the plates. However, since it is located well back from the plasma, disruption loads are substantially reduced and aluminum could be used for the plates. Unlike the FWA, the waveguides are of standard WR187 width. However, the final split of the power from the 12 klystrons is accomplished in the RWA by means of a 3 dB splitter that is formed by slots in the wall between the top two and bottom two waveguides (See Fig. 30.) The measured split of power between the vertically adjacent guides is 3.2 ± .15 dB and the loss of the aluminum waveguides (which are 5.5 mm high compared with ~ 22 mm height of WR 187 guide) is the same as the loss per waveguide in the copper-plated FWA fabricated from stainless steel. As can be seen in Fig. 30, the connection between the sub-height waveguides in the RWA and standard WR 187 waveguide is made by milling an H-plane bend in the top and bottom waveguides to bring the slotted waveguides to the top and bottom surface of the RWA and then expanding the 5.5 mm height to the 22 mm height of WR 187 by means of an E-Plane transformer.

Working forward from the output of each of the 12 klystrons, RF power is brought by 12 WR187 waveguides to the RWA and is there split into 2 branches by means of a power splitter. Each branch carries the power for 2 adjacent sets of 4 vertical waveguides in the FWA. The power in each of these branches is then split again into 2 branches by a four way tee, with one branch feeding the E-plane transformer on a waveguide on the top of the RWA, the other the symmetrical transformer on the bottom. From the transformers, power is coupled into the top and bottom waveguides of the RWA and is split once more

by means of the 3 dB couplers to couple to the middle two waveguides in the RWA. The 8 waveguides at the exit of the RWA excited in this manner by each klystron are then connected to the corresponding waveguides in the FWA and thence to the coupler and plasma. The splitter components connected to the RWA are shown in Fig. 35. Figure 36 shows the splitter in more detail as it appears in the Alcator C-Mod cell.

Aluminum gaskets are used to form the RF seal between the RWA and FWA, and the seals between the FWA and the couplers. Four identical gaskets are used for each joint, one for each row of 24 waveguides. The gaskets are 0.25 mm thick and fabricated by the EDM process. Tight dimensional control in the manufacture of the gaskets and careful alignment of the mating waveguides was required in order to provide adequate gasket compression and to avoid protrusion of the gasket into the waveguide at the joint.

(iv) Launcher Component Tests

The design of each of the main launcher components, i.e., the forward and rear waveguides assemblies and the couplers, has critical issues that can only be verified through a testing program. While testing at low power levels is useful to rule out some of the possible problems such as cross-talk between guides, splitting performance of the 3 dB couplers and insertion loss of the windows, only testing at power levels at or exceeding the nominal operating values can fully verify other design assumptions such as whether the joint between the FWA and RWA will handle the power without arcing at the gasket, or whether the braze compound has sufficiently filled the gap between window and Ti waveguide to prevent arcing in the windows. While the nominal design power is 20 kW per waveguide, corresponding to a total RF power of 2 MW, reflection from the plasma can increase the electric field in the waveguide system to values that correspond to a power several times the nominal value. To verify the performance of the design, a commissioning program was initiated for both individual components and the integrated system. The final acceptance criterion was that the integrated system should pass a minimum of 50 kW per waveguide for 0.5 s into dummy loads mounted at the end of the couplers.

In initial tests, each waveguide in the forward and rear waveguide assemblies was successfully tested at a power level of 50 kW for a pulse length of 0.5 s. The field strength at 50 kW corresponds to 20 kW forward power with a reflection coefficient of magnitude of 0.58. Integrated tests of the FWA and RWA were performed in order to verify the performance of the RF gasket and clamp used to join these assemblies together. Initial tests were unsuccessful due to gasket misalignment and insufficient clamping pressure on the gasket. After correcting these problems, the integrated tests of FWA and RWA were successful in meeting the acceptance criterion of 50 kW/guide for 0.5 s.

The couplers have not been separately tested at high power. However, tests on three-window prototypes have been carried out and were successful in reaching a power level of 100 kW per window for 0.5 s in air at atmospheric pressure.

C. RF Transmitter

RF power is generated by a set of 12 klystrons operating at 4.6 GHz and rated for a CW power of 250 kW each. Varian Associates (now Communications and Power Industries) designed and fabricated the tubes for use in lower hybrid experiments carried out over 20 years ago on the Alcator-C device.[68] The klystrons are cathode switched (no control electrode) and are mounted in groups of 4 on carts. Each of the 3 carts is semi-independently controllable with its own fast-off Transmitter Protection System (TPS) and PLC Controller. Critical protection, control and status information is shared between the transmitter carts and the high-voltage power supply for coordination of overall control tasks. Figure 37 shows the 3 klystron carts installed in the Alcator C-Mod cell above and behind the Waveguide Assembly. The RF output from each klystron is routed to the launcher by rectangular waveguide (WR 187) operating in the TE_{10} mode. The waveguide is pressurized with 10 psig nitrogen at the transmitter. The launcher is separated from the transmitter by both DC breaks ~~blocks~~ and pressure windows.

The klystrons are protected from reflected power by a 4-port ferrite circulator specified for this application and procured from Advanced Ferrite Technology. The circulator is rated to handle 100% reflection at full power over the entire 5-second pulse width with a forward insertion loss of less than 0.2 dB. A high power RF switch allows the RF output to be switched between the waveguides that transmit power to the launcher and an air-cooled dummy load. The waveguide runs are protected from high VSWR or waveguide arcs by both microwave detectors located on directional couplers and by optical arc detectors. The arc detectors are positioned to look directly at the klystron output window and into the circulator.

Protection of the vacuum windows against RF arcs is an important issue and has not yet been resolved. An arc could cause reflected power in a given guide to either increase or decrease, therefore simply using the amplitude of the reflection coefficients in the waveguides as an arc indicator is not sufficient to detect the presence of an arc. An improved strategy would be to compare individual reflection coefficients with an average of those in several neighboring waveguides, an extension of the method used in JET.[77] Another approach would be to monitor the level of 3rd harmonic generation in the guides and use it to trigger a turnoff of the RF power when it exceeds a threshold. However, this approach may be confused by 3rd harmonic generation in the plasma at the mouth of the couplers. Still another approach would be to use light emission on either side of the coupler as an arc indicator. All of these strategies are being developed and one or more of these approaches will be implemented for coupler protection.

(i) High Voltage Supply/Modulator

High voltage is supplied to the klystrons through a single high-voltage power supply/modulator (HVPS) that was specified and procured for this application from Thales Broadcast & Multimedia AG (formally Thomcast AG) of Switzerland.[78] The HVPS is based on Pulse Step Modulation (PSM) technology using 68 individual solid-state switching modules. The switching modules are supplied from 2 cast resin insulated

transformers connected by a circuit breaker to the 13.8 kV mains. The cast resin technology offers many advantages compared to oil insulation, such as the elimination of possible oil leakage and the fire-retardant nature of cast resin. The transformers are phase shifted from each other by 30°, resulting in 12-pulse loading for the mains.

PSM consists in principle of series connected switched mode power supplies, or switching modules (SM), in a buck configuration. Each SM utilizes IGBT semiconductor switching elements and a freewheeling diode. By closing the switching element, the DC voltage of the SM can be switched into the series connection and when switched off the freewheeling diode provides a path for the current to conduct applying only the low forward voltage of the diode. This topology allows the control of the output voltage in step levels. For fine regulation, pulse-width modulation (PWM) at a frequency of 100 kHz is used. This modulation is done with one SM voltage level, but the switching is distributed between the SMs so that a single SM is controlled with a much lower frequency. This results in low switching noise, which can be filtered out easily without adding significant stored energy into the filter circuits.

An additional feature of this technology is the minimal energy storage required to satisfy the requirement of low ripple, thereby eliminating the need for separate modulators and high power crowbars. (A small solid state crowbar is nevertheless required for fast voltage turn off during lightly loaded operation.) The specification required a ripple of less than 0.5% and a short circuit energy release of less than 10 Joules. Both requirements were comfortably met in performance acceptance tests. One disadvantage of supplying the HV from a single supply is that each tube must operate at essentially the same voltage. Nevertheless, small differences in klystron operating voltages can be accommodated by the use of series resistors and variations in output can be regulated by control of the low level drive power.

3.2 Low Level RF Circuitry

The theoretical deposition of lower hybrid driven current depends on the launched $n_\parallel$

spectrum and the plasma temperature profile. Therefore a key consideration in the design of the RF system was to require dynamic control of $n_\parallel$ during the plasma pulse. Such capability could be useful in feedback control of the total current profile, which would be useful in optimizing steady-state performance. In addition, $n_\parallel$ control might be useful in using LHCD to stabilize MHD instabilities such as sawteeth and neoclassical tearing modes.

Since klystrons are amplifiers, dynamic control of their output phase and amplitude is possible at the relatively low level required for their drive. The key components used to implement this feature are I/Q vector modulators (G.T. Microwave, Inc.) and I/Q detectors (MITEQ). A single master oscillator provides the excitation for each klystron through a vector modulator. In open loop mode, I/Q inputs to the vector modulators are determined by operator entry of phase and amplitude setpoints to the control computer. The I/Q detectors monitor the in-phase and quadrature phase components of probe signals picked off from the 12 waveguides carrying power from the klystrons to the launcher. In feedback mode, the I/Q outputs are routed to the control computer where they are compared with demand requests set by the operator, e.g., constant amplitude and uniform $\pi/2$ phase progression.[79] I/Q error signals are generated and processed using PID calculations and the loop is closed by sending the processed error signals on to the vector modulators. In this way, variations due to drift in klystron output amplitude or phase, or waveguide heating, can be essentially eliminated. The overall time response for modifying the $n_\parallel$ spectrum during a plasma pulse is designed to be less than 1 ms. In an advanced mode of operation, the preprogrammed inputs could be replaced by inputs that are based on plasma performance; for example, the rate of phase progression might be controlled by the position of maximum current drive as determined by the hard X-ray camera diagnostic.

D. Launcher Performance and Initial Coupling Studies

In an ideal launcher it would be possible to adjust the phase and amplitude of the 12 splitter inputs to produce a plane of constant phase and amplitude at the interface between

rear and forward waveguide assemblies. In practice, such a constant phase-amplitude plane can only approximately be formed due to path length variations in the splitter network and small tolerance errors in the 3 dB couplers located in the RWA. In our calibration procedure, shims were inserted in the splitter network to reduce the effect of path length variations to a tolerable level, generally within ±5 degrees and ±0.5 dB. Residual phase and amplitude variations were then measured and the results used to calculate the Fourier-transformed launch spectrum as a function of a programmed uniform progression in phase shift. The results are shown in Fig. 38. The measured residual errors give rise to spectra that are nearly indistinguishable from ideal spectra that would have occurred if a perfectly constant phase and amplitude plane had been formed.

In order to produce these spectra at high power, it is necessary to have an accurate mapping of the amplitude and phase produced at each of the splitter inputs vs. the demand settings requested by the operator, which determine the amplitude and phase at each klystron input. The calibration process is carried out by replacing the master oscillator feeding the 12 klystrons by the output of a network analyzer and switching the splitter inputs to matched loads. The input to the network analyzer is taken from directional couplers located just before the splitter input. (The same directional couplers are used to define the phase plane between the FWA and RWA.) Since the response of the I/Q modulator is slightly non-linear, a raster spanning all possible I/Q values is generated and applied to the modulator, and the phase and amplitude at the directional coupler corresponding to each I/Q pair are recorded. The mapping of actual vs. demand values forms a look up table for the control computer to determine the correct I/Q values used to produce a given amplitude and phase at the splitter input for each klystron. The actual values implemented are monitored at the directional couplers by I/Q detectors, and are calibrated by a process similar to that used for the I/Q modulators. While initial experiments have been carried out in an open loop mode, it is planned to eventually close the loop using feedback signals from the I/Q detectors together with demand values developed from signals derived from the plasma, e.g., location of the maximum driven current.

After insertion of the launcher into Alcator C-Mod, the first measurements of the reflection coefficient have been made as a function of phase progression and density at the grill mouth. The latter were made using 6 Langmuir probes embedded in the grill surface (see Fig. 31, right photo.). Forward and reflected powers at 48 directional couplers located just before the E-plane transformers feeding the RWA were measured and their ratios were computed to form 48 reflection coefficients. These were then averaged in order to determine a single global reflection coefficient. The measurements were made at a relatively low applied power in the range 100-200 kW. The dependence of the global reflection coefficient as a function of phase and density at the launcher mouth as a parameter is shown in Fig. 39. It can be seen that excellent coupling efficiency (6% reflection) has been obtained at a relatively high density at the grill ($\sim 3 \times 10^{18}$ m^{-3}) and at optimal current drive phasing (90°).

Unfortunately, initial LH experiments had to be terminated due to interactions of the titanium grill with hydrogen that led to loss of material from the couplers. New couplers made from stainless steel have been fabricated; when installed, lower hybrid experiments will resume with emphasis on raising the power to the MW level as required for significant current drive.

VII. Summary

This paper has reviewed physics and technology research in the area of wave-particle interactions in the ion cyclotron and lower hybrid range of frequencies on the Alcator C-Mod tokamak. The first part of the paper described the design and fabrication of three ICRF antennas installed in C-Mod. Physics and technological issues related to successful operation of these antennas in the severe high power conditions typical of C-Mod plasmas were reviewed, including details of the Faraday screen design and manufacture. Design and operation of the two-strap D- and E- antennas benefited greatly from extensive experience on other tokamak experiments and these antennas have routinely achieved power densities of 10 MW/m^2 without significant impurity generation problems. After an extensive design and development program, the four strap J-antenna was also operated successfully with surface power densities exceeding 11 MW/m^2 and comparable impurity generation. Operation of the four FMIT transmitters at the 2 MW output power level and in the 40 – 80 MHz range was also described. Critical issues related to prolonging tube lifetime such as tube arc protection were discussed. It was reported that tube filament hours could be increased from $\approx$ 1000 to $\approx$ 2500 – 2700 hours through protective measures such as tube screen protection. A transmission system for the ICRF system was also described which employs mechanical phase shifters and stub tuners. Presently, the tuning of this system is manual with between discharge tuning.

Initially, ICRF physics research on C-Mod concentrated primarily on the study of minority heating schemes in the strong single pass damping regime (H-minority in D) and in the weak single pass damping case (^{3}He minority in D). The dependence of overall heating efficiency with minority concentration was carefully documented and the highest stored energies ever produced on C-Mod were ultimately achieved with H-minority heating. Second harmonic minority heating schemes in H and D were also explored however poor plasma heating was observed in these discharges owing to the weak single pass damping. Localized electron heating via mode converted ICRF was studied next in both two ion species plasmas (^{3}He in D) and three species plasmas (D-H-

[3]He).   Fundamental detection measurements of mode converted ion Bernstein and ion cyclotron waves were also reported on C-Mod using a Phase Contrast Imaging (PCI) diagnostic. Massively parallel simulations of these mode conversion experiments were also reported along with the development of a synthetic diagnostic to interpret the PCI measurements.   Recent experiments on sawtooth modification via localized mode conversion current drive (MCCD) were described. In these experiments the MCCD was believed to be reducing the local shear at the q=1 surface and therefore stabilizing sawteeth.   Experimental results were also reported where the sawtooth period was extended (stabilized) via energetic particle production during H-minority heating.

The final part of this paper described the LH current profile control program that is now starting up on C-Mod. The physics basis for the program was reviewed, emphasizing the use of off-axis LHCD to produce reversed shear profiles.   The stability properties of discharges near the ideal, no-wall β-limit were described and it was shown that for modest increases in the confinement enhancement factor (H $\approx$ 2.5) it is possible to produce plasmas with 70% non-inductive bootstrap current with the remaining current being provided by off-axis LHCD.   It is anticipated that this off-axis current profile control capability will also be beneficial for stabilizing sawteeth and perhaps even for stabilizing NTM's.

In the final section of this paper a new lower hybrid system implemented on Alcator C-Mod was described. The system features a single 4x24 waveguide launcher driven by 12 independently controllable klystrons with a total source power of 3 MW. The system has the capability of delivering up to 2 MW to C-Mod plasmas A unique feature is the ability to dynamically vary the applied $n_\parallel$ spectrum over the range $1.5 < n_\parallel < 3$ with a time response of about 1 ms. This flexibility will be exploited in controlling the absorption radius of the LH waves and thereby the location of the LH driven current, a capability that may be important in producing and sustaining optimized steady-state regimes in tokamaks. A second grill and an additional megawatt of power is planned to be added in a second phase, which will increase the overall LH system flexibility.

Preliminary measurements of the coupling at relatively low power (100-200 kW) show excellent absorption of the launched lower hybrid waves with a reflection coefficient as low as 6%. Initial measurements had to be terminated due to hydrogen interactions with the titanium couplers. New couplers have been fabricated from stainless steel. When installed, lower hybrid experiments will resume with the emphasis on increasing the power to the MW level required for significant current drive.

References

[1] "Multi-Phase Cooled Power Tetrode 4CM2500KG", CPI Eimac Division (1999) and "8973 Water Cooled Power Tetrode", Varian Eimac (1985).

[2] A. Parisot, S.J. Wukitch, P. Bonoli et al., Plasma Physics and Controlled Fusion **46**, 1781 (2004).

[3] A. Parisot, S. Wukitch, Y. Lin et al., 31st EPS Conference on Plasma Physics (ECA), **28G**, P-2.168 (2004).

[4] D. Swain, R. Goulding, Y. Lin et al., 23rd Symposium on Fusion Technology (Venice, Italy, 2004) Paper PST-B-460.

[5] F. Braun and W. Arnold, 18th Symposium on Fusion Engineering (Albuquerque, NM, 1999) IEEE 395 (1999).

[6] F. Braun, F. Hofmeister, F. Wesner et al., Fusion Engineering and Design **56-57**, 551 (2001).

[7] Y. Takase, S. Golovato, M. Porkolab, K. Bajwa, H. Becker, and D. Caldwell, Fusion Engineering **1**, 118 (1992).

[8] S.N. Golovato, W. Beck, P. Bonoli, M. Fridberg, M. Porkolab, and Y. Takase, Fusion Engineering **2**, 1069 (1994).

[9] G. Schilling, J. Hosea, J.R. Wilson et al., AIP Conference Proceedings **485**, 429 (2001).

[10] S.J. Wukitch, R. Boivin, P.T. Bonoli et al., Plasma Physics and Controlled Fusion **46**, 1479 (2004).

[11] F.W. Perkins and R.F. Kluge, IEEE Transactions on Plasma Science **PS-12**, 161 (1984).

[12] H. Kimura, T. Imai, and T. Yamamoto, Nucl. Fusion **35**, 619 (1997).

[13] T. Graves et al., submitted to J. Vacuum Science and Technology 2005.

[14] J. Adam and Equipe TFR, Plasma Physics and Controlled Fusion **26**, 165 (1984).

[15] H. Ogawa, K. Odajima, H. Ohtsuka et al., Journal of Nuclear Materials **128-129**, 298 1984).

[16] N. Noda, T. Watari, K. Toi et al., Journal of Nuclear Materials **128-129**, 304 (1984).

[17] P.L. Colestock, S.A. Cohen, J.C. Hosea, D.Q. Hwang, G.J. Greene, J.R. Wilson, M. Ono, D. Manos, R. Budny, G. Hammet, and R. Kaita, Joournal of Vacuum Science and Technology A **3**, 1211 (1985).

[18] J. Adam, Plasma Physics and Controlled Fusion **29**(4), 443 (1987).

[19] P. Colestock, G.J. Greene, J.C. Hosea, C.K. Phillips, J.E. Stevens, M. Ono, J.R. Wilson, D.A. D'Ippolito, J.R. Myra, and I.S. Lehrman, Fusion Engineering Design **12**, 43 (1990).

[20] J.-M. Noterdaeme and the ASDEX-team ICRH-team, NI-team, Fusion Engineering Design **12**, 127 (1990).

[21] T. Fujii, K. Odajima, H. Ohtsuka, H. Matsumoto, H. Kimura, M. Ono, K. Tobita, M. Nemoto, Y. Kusama, M Seki, S. Moriyama, T. Nishitani, H. Nakamura, H. Takeuchi, K. Annoh, S. Shinozaki, M. Terakado, and JT-60 Team, Fusion Engineering Design **12**, 139 (1990).

[22] G. Van Oost, R. Van Nieuwenhove, R. Koch, A.M. Messiaen, R.R. Weynants, K.H. Dippel, K.H. Finken, Y.T. Lie, A. Pospieszczyk, U. Samm, B. Schweer, R.W. Conn, W.J. Corbett, D.M. Goebel, and R.A. Moyer, Fusion Engineering Design **12**, 149 (1990).

[23] B. Lipschultz, D.A. Pappas, B. LaBombard, J.E. Rice, D. Smith, and S.J. Wukitch *et al.*, Nuclear Fusion **41**, 585 (2001).

[24] D.A. D'Ippolito, J.R. Myra, M. Bures, and J. Jacquinot, Plasma Physics and Controlled Fusion **33**, 607 (1991).

[25] M. Bures, J. Jacquinot, K. Lawson, M. Stamp, H.P. Summers, D.A. D'Ippolito, and J.R. Myra, Plasma Physics and Controlled Fusion **33**, 937 (1991).

[26] B. Lipschultz *et al.*, submitted to Physics of Plasmas (2005).

[27] M. Greenwald, R.L. Boivin, F. Bombarda *et al.*, Nuclear Fusion **37**, 793 (1997).

[28] Y. Takase, R.L. Boivin, F. Bombarda *et al.*, Physics of Plasmas **4**, 1647 (1997).

[29] T. H. Stix, Nuclear Fusion **15**, 737 (1975).

[30] M. Porkolab, in Advances in Plasma Physics, AIP Conference Proceedings 314, Ed. N. Fisch, (AIP, NY, 1994), p. 99.

[31] ITER Physics Design Guidelines: 1989, N. Uckan, and the ITER Physics Group (IAEA, Vienna, 1990) ITER Documentation Series No. 10.

[32] P.J. O'Shea, P. Bonoli, A.E. Hubbard, M. Porkolab, and Y. Takase, Bulletin of the American Physical Society **41**, 1548 (1996).

[33] G.W. Hammett, "Fast Ion Studies of Ion Cyclotron Heating in the PLT Tokamak", PhD Dissertation, University Microfilms International No. GAX86-12694, Princeton University (1986).

[34] M. Brambilla, Plasma Physics and Controlled Fusion **41**, 1 (1999).

[35] R. Hawryluk, in Physics of Plasmas Close to Thermonuclear Conditions, Eds. B. Coppi, G.G. Leotta, D. Pfirsch, R. Pozzoli, and E. Sindoni (CEC, Brussels, 1980), Document EUR FU BRU/XII/476/80 p. 19.

[36] S.J. Wukitch, P.T. Bonoli, E. Nelson-Melby *et al*, in Proceedings of the 25th Conference on Controlled Fusion and Plasma Physics, Prague, 1998 Eds. J. Badelec, J. Stockel, P. Sunka, M. Tendler, (EPS, Brussels, 1998), Paper P3.020.

[37] L.L. Lao, H. St. John, R. Stambaugh, A.G. Kellman, and W. Pfeiffer, Nuclear Fusion **25**, 1611 (1985).

[38] P.T. Bonoli, S.N. Golovato, P. O'Shea *et al*., Proceedings of the 16th IAEA Conference on Fusion Energy (Montreal, Canada), (IAEA, Vienna, 1996) Vol. 3, p. 309.

[39] P.T. Bonoli, P. O'Shea, M. Brambilla *et al*, Physics of Plasmas, **4**, 1774 (1997).

[40] E. Nelson-Melby, M. Porkolab, P.T. Bonoli, Y. Lin, A. Mazurenko, and S.J. Wukitch, Physical Review Letters, **90**, 155004 (2003).

[41] Y. Lin, S. Wukitch, P.T. Bonoli *et al*., Physics of Plasmas **11**, 2466 (2004).

[42] M. Porkolab, P.T. Bonoli, L. Lin *et al*, 20th IAEA Energy Fusion Conference, Vilamoura, Portugal, November, 2004, Paper IAEA-CN-116/EX/P4-32.

[43] Y. Lin, S. Wukitch, A. Parisot *et al*, Plasma Physics and Controlled Fusion **47**, 1207 (2005).

[44] P.T. Bonoli, M. Brambilla, E. Nelson-Melby *et al*, Physics of Plasmas **7**, 1886 (2000).

[45] J.C. Wright, P.T. Bonoli, M. Brambilla *et al*, Physics of Plasmas **11**, 2473 (2004).

[46] P.J. O'Shea, "Measurements of ICRF Power Deposition and Thermal Transport with an ECE Grating Polychromator on the Alcator C-Mod Tokamak", Doctoral Thesis, Massachusetts Institute of Technology, 1997.

[47] M. Brambilla, Nuclear Fusion **38**, 1805 (1998).

[48] H. Weisen, Review of Scientific Intruments **59**, 1544 (1988).

[49] S. Coda, M. Porkolab, and T.N. Carlstrom, Review of Scientific Instruments **63**, 4974 (1992).

[50] A. Mazurenko, M. Porkolab, D. Mossessian *et al.*, Physical Review Letters **89**, 225004 (2002).

[51] A. Mazurenko, "Phase Contrast Imaging on the Alcator C-Mod Tokamk", PhD Dissertation, Massachusetts Institute of Technology Department of Physics (2001).

[52] F.W. Perkins, Nuclear Fusion **17**, 1197 (1977).

[53] E.F. Jaeger, L.A. Berry, J.R. Myra *et al.*, Physical Review Letters **90**, 155001 (2003).

[54] J.W. Heard, C. Watts, R.F. Gandy, and P.E. Phillips, Review of Scientific Instruments **70**, 1011 (1999).

[55] Y. Lin, S.J. Wukitch, P.T. Bonoli *et al.*, Plasma Physics and Controlled Fusion **45**, 1013 (2003).

[56] T.E. Tutt, Department of Nuclear Engineering Master's Thesis, Massachusetts Institute of Technology (1999).

[57] V.P. Bhatnagar, D.F.H. Start, J. Jacquinot, F. Chaland, A. Cherubini, and F. Porcelli Nuclear Fusion **34**, 1579 (1994).

[58] F. Porcelli, D. Boucher, and M.N. Rosenbluth Plasma Physics and Controlled Fusion **38**, 2163 (1996).

[59] S.J. Wukitch, Y. Lin, A. Parisot *et al.*, Physics of Plasmas **12**, 056104 (2005).

[60] P.T. Bonoli, J.C. Wright, Y. Lin, M. Porkolab, S.J. Wukitch, E. D'Azevedo, and M. Brambilla, Bulletin of the American Physical Society **47**, 141 (2002).

[61] D.A. Ehst and C.F.F. Karney Nuclear Fusion **31,** 1933 (1991).

[62] R. Majeski, J.H. Rogers, S.H. Batha *et al.*, Physics of Plasmas **3**, 2006 (1996).

[63] R. Majeski, J.H. Rogers, S.H. Batha *et al.*, Physical Review Letters **76**, 764 (1996).

[64] J.A. Snipes, N. Basse, C. Boswell *et al*, Physics of Plasmas **12**, 056102 (2005).

[65] P.T. Bonoli, M. Porkolab, J. Ramos, W. Nevins, and C. Kessel, Plasma Physics and Controlled Fusion **39**, 223 (1997).

[66] P.T. Bonoli, R.R. Parker, M. Porkolab, J.J Ramos, S.J. Wukitch, Y. Takase, S. Bernabei, J.C. Hosea, G. Schilling, J.R. Wilson, Nulcear Fusion 40, 1251 (2000).

[67] S.C. Jardin, C.E. Kessel, C.G. Bathke *et al*, Fusion Engineering and Design **38**, 27 (1997).

[68] M. Porkolab, J.J. Schuss, B. Lloyd *et al*., Physical Review Letters **53**, 450 (1984).

[69] R.S. Devoto, D.T. Blackfield, M.E. Fenstermacher, P.T. Bonoli, M. Porkolab, and G. Tinios, N"uclear Fusion **32**, 773 (1992).

[70] J. Delucia, S.C. Jardin, and A.M.M. Todd, Journal of Computational Physics **37**, 183 (1980).

[71] R.C. Grimm, R.L. Dewar, and J. Manickam, Jouranl of Computational Physics **49**, 94 (1983).

[72] A.D. Turnbull, T.S. Taylor, M.S. Chu, R.L. Miller, and Y.R. Lin-Liu, Nuclear Fusion **38**, 1467 (1998).

[73] "The CQL3D Fokker-Planck Code", R.W. Harvey and M.G. McCoy, Proceedings of the IAEA Technical Committee Meeting on Advances in Simulation and Modeling of Thermonuclear Plasmas, Montreal, 1992, p. 489-526, IAEA, Vienna (1993).

[74] A.P. Smirnov and R.W. Harvey, Bulletin of the American Physical Society **40**, 1837 (1995).

[75] S. Bernabei, J.C. Hosea, C.C. Kung *et al*., Fusion Science and Technology **43**, 145 (2003).

[76] J. Hosea, D. Beals, W. Beck, *et al*., Proceedings of the 20th Symposium on Fusion Technology (SOFT), Venice, (2004).

[77] G. Ekedahl, G. Granucci, J. Mailloux *et al*., Nuclear Fusion **45**, 351 (2005).

[78] M. Grimes, D. Gwinn, R. Parker *et al*., Proceedings of the 19th IEEE/NPSS Symposium on Fusion Engineering (SOFE), Atlantic City, NJ, 16 (2002).

[79] D. Terry, W. Burke, M. Grimes et.al., Proceedings of the 20th IEEE/NPSS Symposium on Fusion Engineering (SOFE), San Diego, CA, 524 (2003).

Table 1. Alcator C-Mod RF Heating and Current Drive Systems

Ion Cyclotron Heating System

	Phase I *Present Capability*		*Phase II*
	D- and E- Antenna	J - Antenna	D- and E- Antennas
Frequency	80 MHz	50-80 MHz	50-80 MHz
Power (Source)	2 MW each	4 MW	4 MW each
Antenna	2 Straps each	4 Straps	4 Straps each

Lower Hybrid Current Drive System

	Phase I *Present Capability*	*Phase II*
Frequency	4.6 GHz	4.6 GHz
Power (Source)	3 MW	4 MW
Antenna	4X24 Waveguide Grill (1)	4X24 Waveguide Grills (2)
$N_{||}$ (Variable)	1.5-3	1.5-3

Figure Captions

Figure 1: View of the D- and E- dipole antennas in Alcator C-Mod showing the current straps and Faraday screens.

Figure 2: View of the four strap J - antenna in Alcator C-Mod showing the current straps and Faraday screen.

Figure 3: An example of high power ICRF hydrogen minority heating in Alcator from the 2005 campaign with ICRF power injected from the D-, E-, and J- antennas [B_T=5.4 T, I_P=1.0 MA].

Figure 4: ICRF hydrogen minority heating from an earlier campaign in Alcator (1996) with 2.8 MW of ICRF power at 80 MHz was injected from the D- and E- two strap antennas [B_T=5.3 T, I_P=1.0 MA].

Figure 5: Analysis of ICRF heating at 0.9 sec. for the discharge shown in Fig. 4 using the TORIC full-wave ICRF solver. (a) Radial power deposition profiles predicted by TORIC for the minority hydrogen damping (triangles), second harmonic deuterium damping (diamonds), direct electron Landau damping (squares), and total (circles). (b) Contours of the left circularly polarized electric field computed by TORIC.

Figure 6: Fokker Planck analysis of the ICRF power partition at 0.9 sec. for the discharge shown in Fig. 3, using the FPPRF code. (a) Radial heating profile due to the minority ion tail predicted by FPPRF. Circles correspond to the minority tail heating to electrons via drag and squares correspond to the minority heating to background ions via collisions. (b) Radial profile of the minority tail temperature [2/3<E>]. Shown for reference is the radial profile of the background electron temperature.

Figure 7: Scan of overall heating efficiency versus hydrogen concentration during ICRF minority heating in Alcator C-Mod. Heating efficiency was determined by analyzing the break in slope in the stored energy associated with an RF transition.

Figure 8: An example of D(^{3}He) minority heating in an ELM-free H-mode discharge in Alcator C-Mod [P_{ICRF} = 2.4 MW and I_P = 1.2 MA].

Figure 9: Scan of the overall heating efficiency for the D(^{3}He) minority heating scheme versus (^{3}He) concentration. The heating efficiency is again obtained from a break in slope analysis of the stored energy at a transition in the RF power.

Figure 10: Comparison of the performance of the two strap (D- and E-) and four strap (J-) antennas during ICRF minority hydrogen heating in a single C-Mod discharge [B_T=5.2 T, I_P=0.8 MA].

Figure 11: Comparison of the J-antenna performance operated with current drive phasing $(0,\pm\pi/2,\pm\pi,\pm3\pi/2)$ and heating phasing $(0, \pi, \pi, 0)$, using three identical L-mode target plasmas [B_T=5.2 T, I_P=0.8 MA].

Figure 12: An example of off-axis mode conversion electron heating (MCEH) in Alcator C-Mod, deduced using a break in slope method on the electron temperature versus time [B_0 = 7.9T, I_P=1.2 MA, $n_e(0) \approx 2.5 \times 10^{20}$ m^{-3}, n_{He-3} / $n_e \cong 0.24$, n_D / $n_e \cong 0.05$, and n_D / $n_e \cong 0.47$]. (a) Time traces of the central and off-axis electron temperature channels at a single RF transition. (b) Radial profile of MCEH associated with the RF transition in (a).

Figure 13: Mode conversion electron heating versus ^{3}He concentration in C-Mod discharges, deduced using the break in slope method. Experimental data with error bars corresponds to crosses. Shown for comparison are the predictions for MCEH from the TORIC full-wave spectral solver (open and closed diamonds) using 15 and 255 poloidal modes.

Figure 14: Contours of the left circularly polarized electric field from a TORIC simulation in Fig. 13, corresponding to $n_{He-3} / n_e = 0.24$, 255 poloidal modes, and 480 radial elements. This simulation was performed with a parallel version of the TORIC field solver on the MIT MARSHALL cluster.

Figure 15: Schematic layouts of the phase contrast imaging (PCI) diagnostic in Alcator C-Mod. (a) The Alcator C-Mod tokamak cross-section with the PCI laser path and the RF antenna location. (b) Top (toroidal) view of the PCI diagnostic location, relative to the D-, E-, and J- antenna locations.

Figure 16: (a) 2D Fourier transform of the PCI data, showing the presence of an ion cyclotron wave (ICW) at the expected RF heterodyne frequency of 350.9 kHz. (b) $n_\perp^2 = (k_\perp c/\omega)^2$ versus $(R - R_0)$ for the fast magnetosonic wave (FW), ion cyclotron wave (ICW), and ion Bernstein wave (IBW). Also shown are the FW cut-off at $n_{//}^2 = L$ and the mode conversion layer at $n_{//}^2 = S$.

Figure 17: Line integrated PCI signal is plotted versus major radial position (R). The magnetic axis is located at 67 cm and the ion-ion hybrid layer is located to the high field side of the plot at 57 ± 2cm.

Figure 18: Example of an ICW simulation in Alcator C-Mod using the TORIC full-wave solver. Plasma parameters used in this simulation were 21% D, 23% ^{3}He, and 33% H, n_ϕ = 13, 240 radial elements, and 255 poloidal modes. Contours of the Re($E_{//}$) have been plotted.

Figure 19: (a,b) Contours of fluctuating electron density computed from the TORIC electric field solutions for off-axis ICRF mode conversion in C-Mod. (c) Comparison of the mode conversion direct electron heating profiles in the C-Mod experiment with profiles computed by TORIC under different assumptions for the ^{3}He concentration.

Figure 20: Experimental and synthetic PCI line integrated density fluctuation amplitude versus major radius for the discharge simulated in Fig. 19. (a) Real part, (b) imaginary part, and (c) magnitude.

Figure 21: On-axis mode conversion in D(H) plasmas in Alcator C-Mod. (a) Experimental electron heating profiles from a break in slope method. The electron heating profile and minority heating profile from TORIC are also shown [19% H, 81% D, and f_{rf} = 70 MHz. The shaded area is the 'noise floor' level of the break-in-slope method. (b) Electron heating contours (with enlargement to the right) from a TORIC simulation (n_ϕ = 13) of the on-axis mode conversion case in (a). The lowest contour level of the left figure is omitted.

Figure 22: Off-axis mode conversion in D(H) plasmas in Alcator C-Mod. (a) Experimental electron heating profiles from a break in slope method. The electron heating profile and minority heating profile from TORIC are also shown [22.5% H, 77.5% D, and f_{rf} = 80 MHz. (b) Electron heating contours (with enlargement to the right) from a TORIC simulation (n_ϕ = 10) of the on-axis mode conversion case in (a). The lowest contour level of the left figure is omitted.

Figure 23: Sawtooth modification via localized ICRF mode conversion current drive in Alcator C-Mod. (a) RF power traces for two discharges where the antenna phase was changed from ctr- to co-CD phasing. The sawtooth period is lengthened for the ctr-CD case (left panel) and shortened for the co-CD case (right panel) consistent with increasing the sawtooth period by lowering the shear at the q=1 surface. (b) The co- and ctr-current drive power deposition profiles from a single RF transition for the cases shown in (a).

Figure 24: Enlargement of the central electron temperature versus time for three identical L-mode target plasmas [B_T=5.2 T, I_P=0.8 MA] heated with the J- antenna operated with current drive phasing $(0,\pm\pi/2,\pm\pi,\pm3\pi/2)$ and heating phasing $(0, \pi, \pi, 0)$.

Figure 25: ACCOME simulation results for lower hybrid current profile control in a highly shaped C-Mod discharge ($\kappa_\chi = 1.77$ and $\delta_\chi = 0.71$) with a broad pressure profile [$p(0)$ / p_{avg} =2.90]. (a) Current density profiles (MA / m^2) versus normalized square root toroidal flux (ρ). (b) Profile of the safety factor (q) versus ρ.

Figure 26: Flux contours for the highly shaped C-Mod equilibrium (κ_χ **= 1.77 and** $\delta_\chi =$ 0.71) corresponding to the ACCOME simulation in Fig. 25.

Figure 27: Stability limit against the n=1 external kink mode in the absence of conducting walls, in an $\varepsilon\beta_p$ versus q_* space spanned by scaling the ACCOME equilibrium with broad profiles depicted in Figure 25. The location of the original equilibrium is indicated by the red triangle and the stable domain is below the curve. The red square is a similar reversed shear equilibrium simulated with ACCOME that was reported in Ref. [60]. Mode resonant values of q_{min} along the marginal stability curve are indicated by arrows. Also shown for reference is the stability boundary with a conducting wall placed at 1.3a.

Figure 28: H-Mode discharge produced in Alcator C-Mod with lower density and higher temperature [$P_{ICRF} = 3.4$ MW, $B_0 = 5.4$T and $I_p = 0.6$ MA]. Discharge is a possible target plasma for LH current drive studies. (a) Measured density profile versus poloidal flux at 1.045 sec. (b) Measured electron temperature profile versus poloidal flux at 1.045 sec.

Figure 29: Lower hybrid (LH) wave absorption and current generation computed with the CQL3D – GENRAY codes using the density and temperature profiles in Fig. 28. The LH parameters were $P_{LH} = 3.0$ MW, $n_{//}(0) = 2.50$ in the co-current drive direction, and f_0 = 4.6 GHz. (a) Radial profile of the LHRF power deposition (W/cm^3) versus normalized radius (ρ). (b) Radial profile of the LHRF current density (A/cm^2) versus normalized radius (ρ).

Figure 30: Cross-sectional drawing of the LHCD launcher assembly mounted in an Alcator C-Mod port.

Figure 31: Photographs of the four couplers before (left) and after (right) installation into Alcator C-Mod. Six Langmuir probes embedded in the surfaces of the launcher between the couplers are visible in the photo on the right.

Figure 32: Schematic of the way power from each of 12 klystrons is divided in order to feed 2 adjacent columns of the grill. The low level phase shifter and attenuator is electronically controlled.

Figure 33: Figure 4. Views of one of the four couplers. The ceramic windows after brazing are clearly shown in the left panel, while an additional ceramic strip brazed on the outside wall to reduce stresses in the outer windows is shown on the right.

Figure 34: Photograph of the copper plated forward waveguide assembly (FWA).

Figure 35: Rear LH waveguide assembly and splitter network.

Figure 36: Splitter network as installed on the Alcator C-Mod tokamak.

Figure 37: Photograph of the klystron carts installed in the Alcator C-Mod cell. Four klystrons are mounted in each cart.

Figure 38: Calculated $n_{\parallel}$ spectra of the four waveguide rows A-D, as a function of waveguide-to-waveguide phase progression. Small residual phase and amplitude errors have been taken into account.

Figure 39: Global reflection coefficient vs. waveguide phasing. In obtaining these data the mechanical phase shifter was fixed at ± 90°, where the + sign corresponds to the co-current drive (CD) direction, the – sign to the counter current drive direction (CCD). Thus a uniform phase progression occurs only at 90°. The densities corresponding to 1,3

and 5 mm (distance from limiter) vary over the face of the grill, and are in the ranges 2.5-3.5x10^{18}, 0.8-1.3x10^{18} and 2-3x10^{17} m^{-3} respectively.
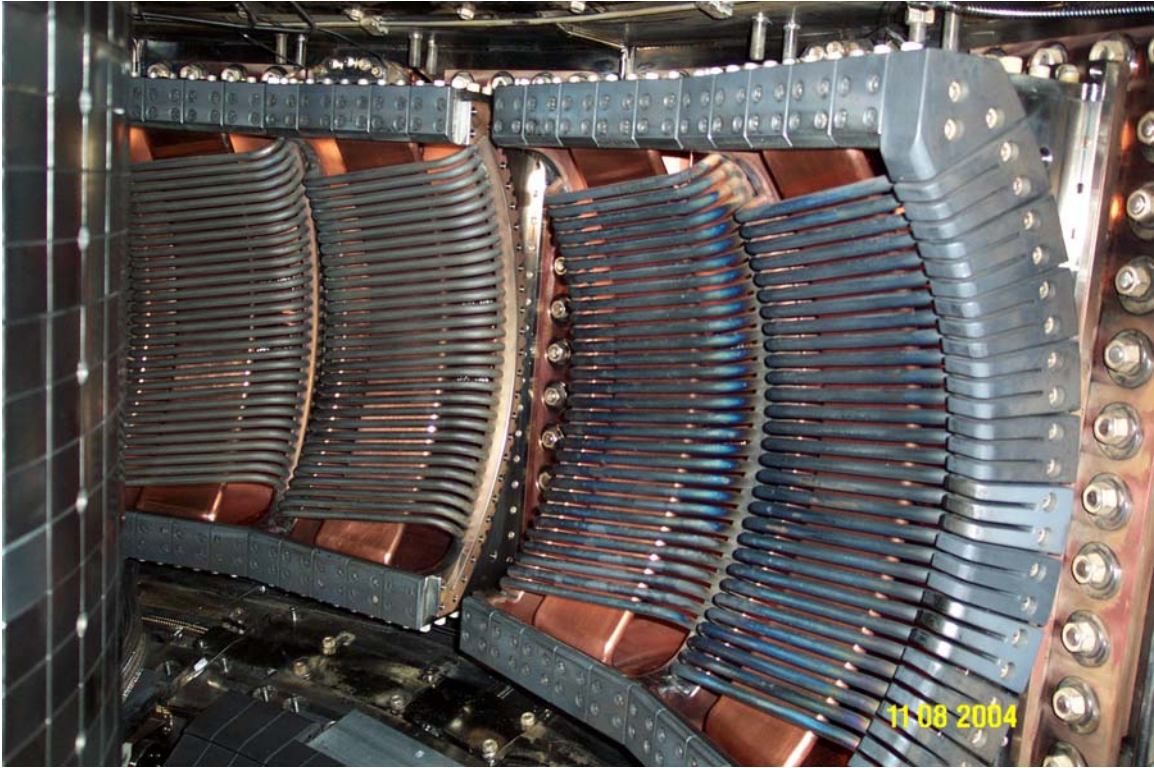
Figure 1

Figure 2

Figure 3

Figure 4

RF Power Deposition Profiles

Figure 5(a)

Re(E)
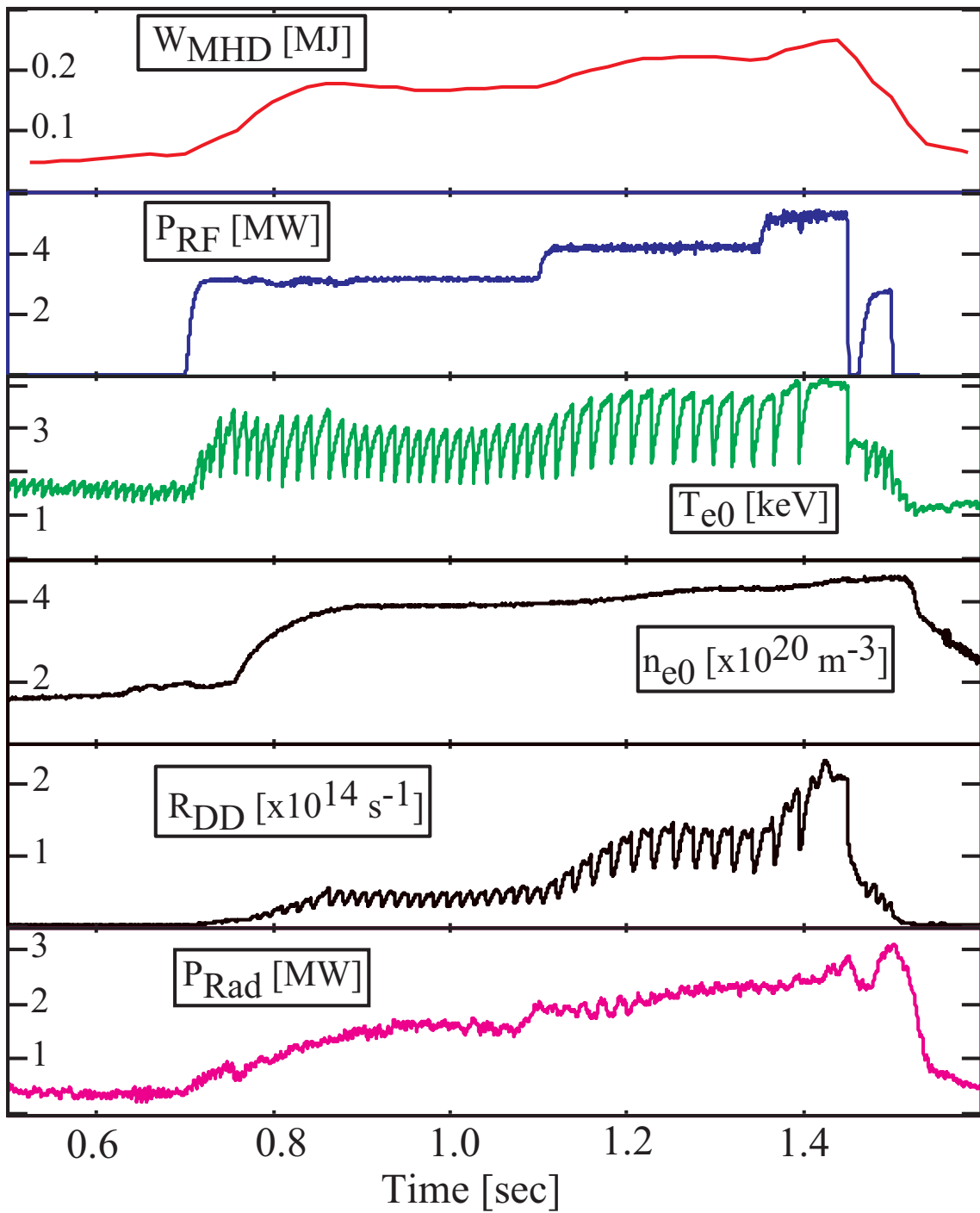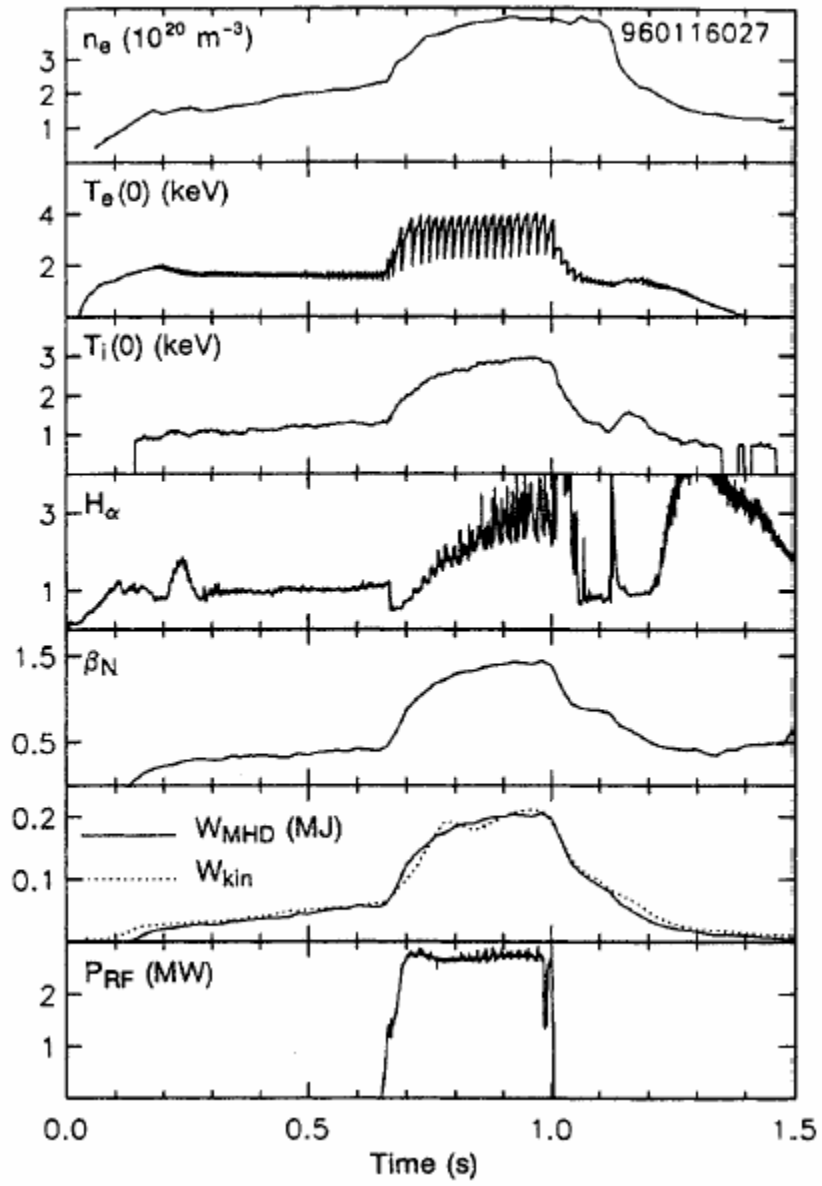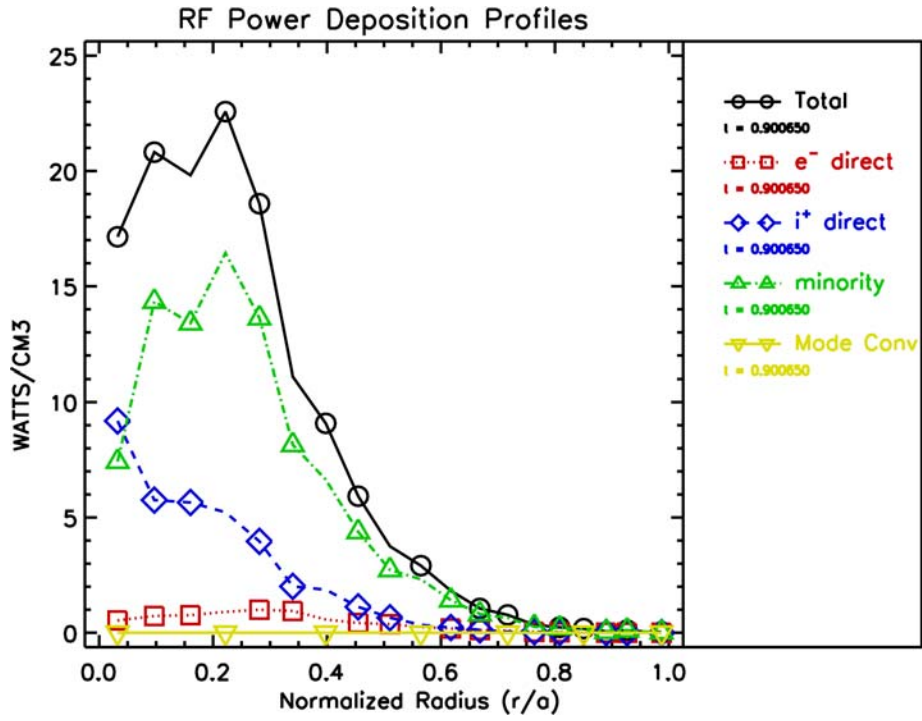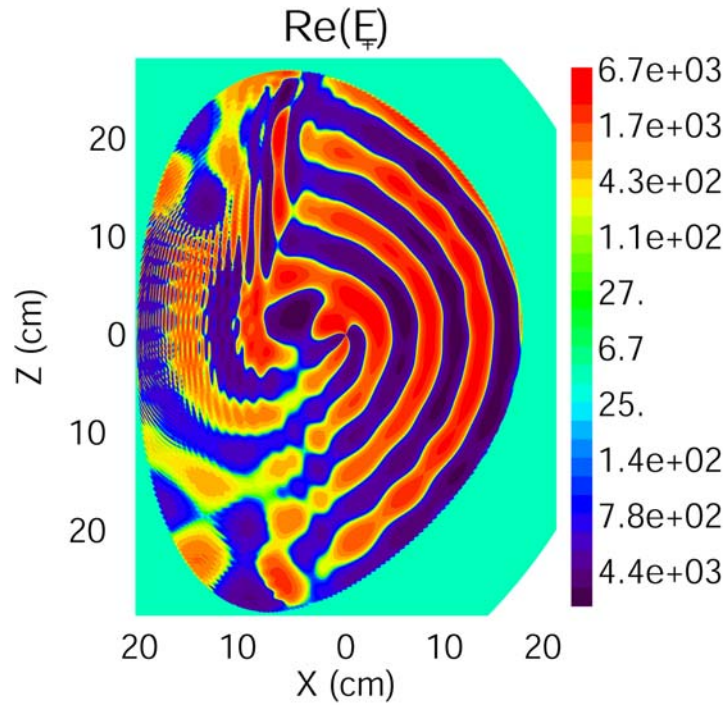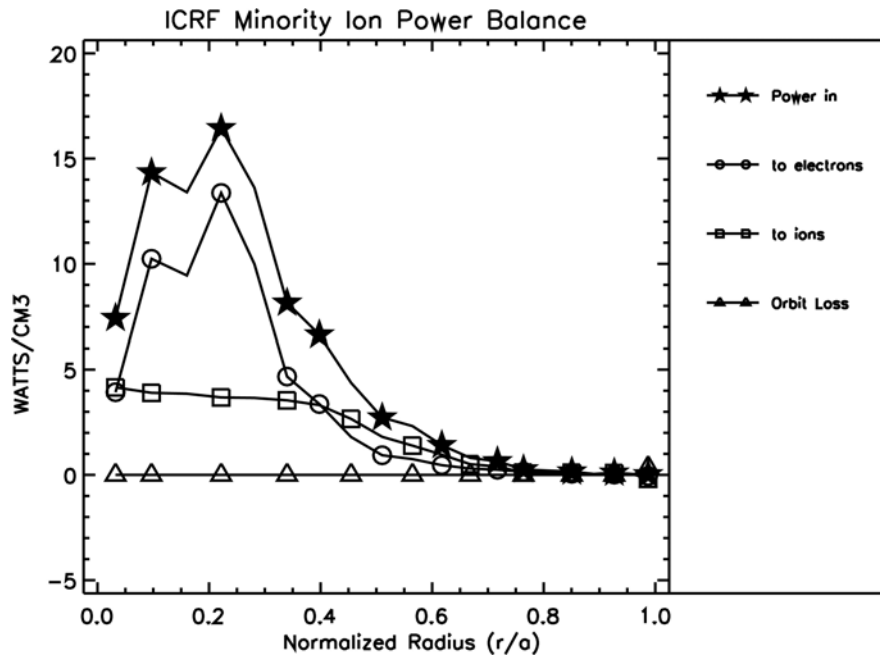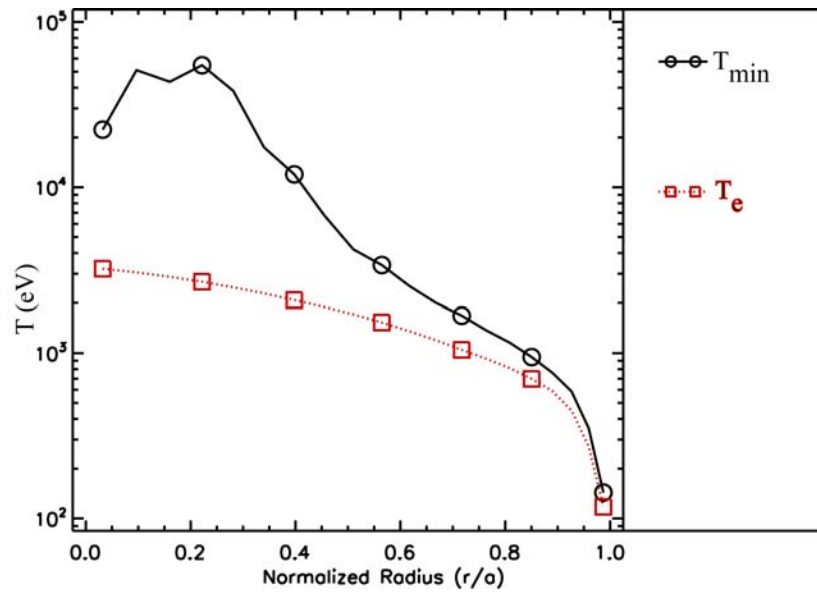
Figure 5(b)

Figure 6(a)

Figure 6(b)
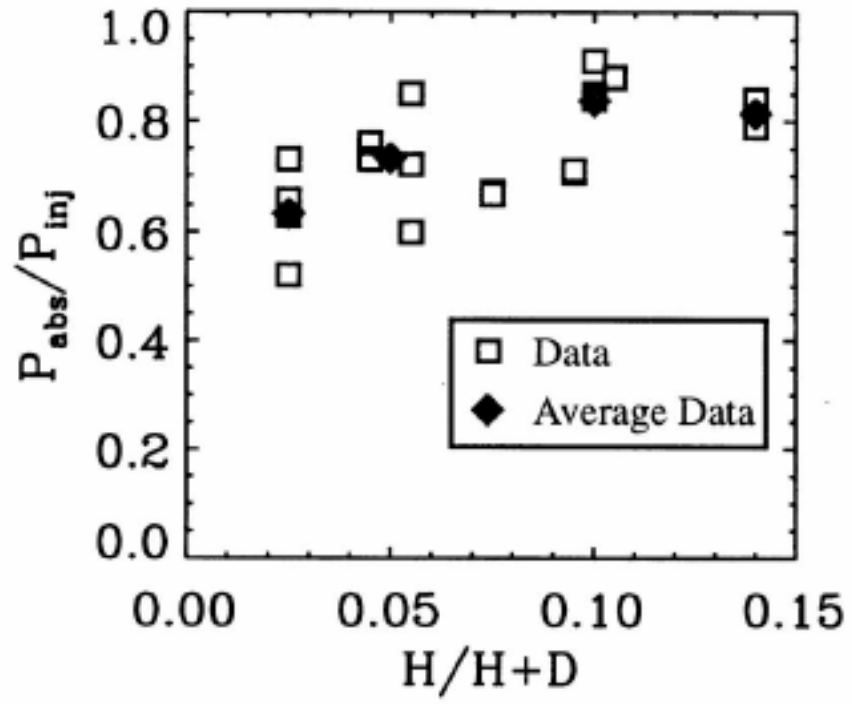
Figure 7
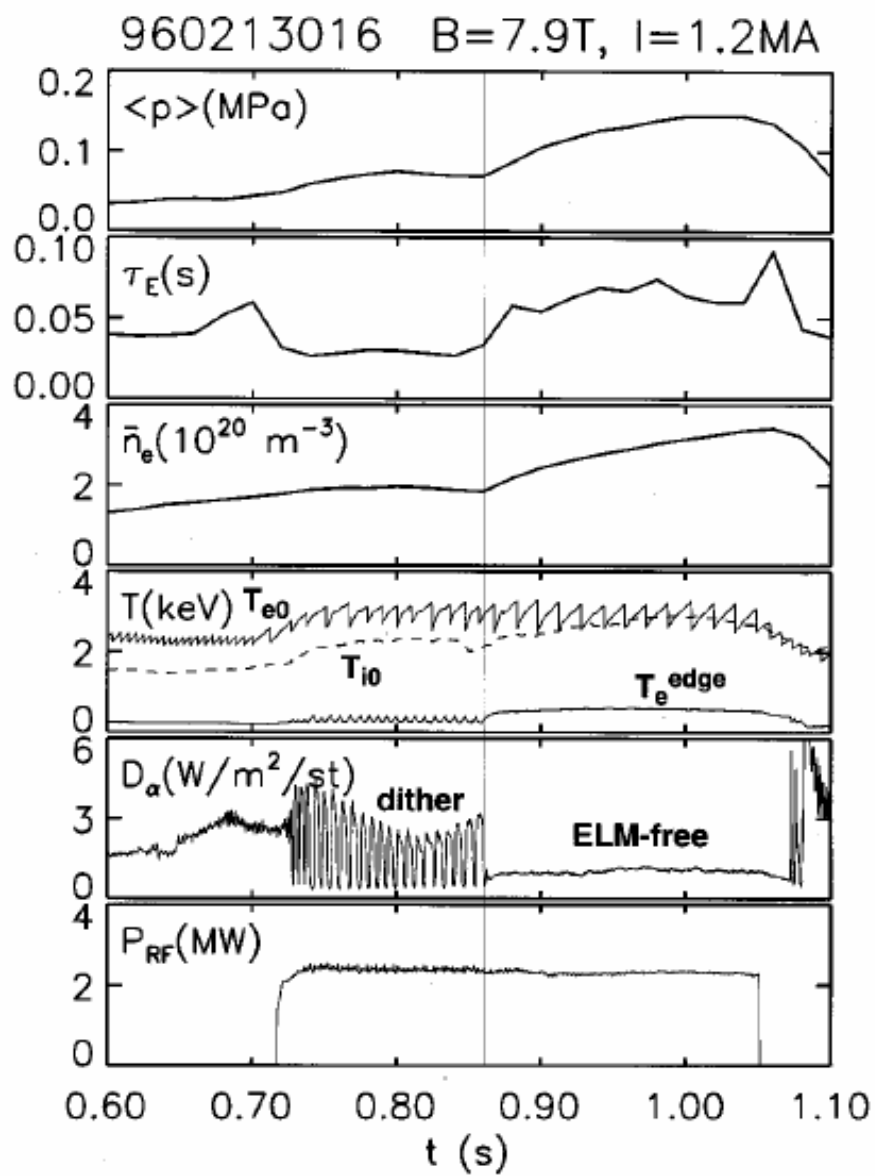
Figure 8
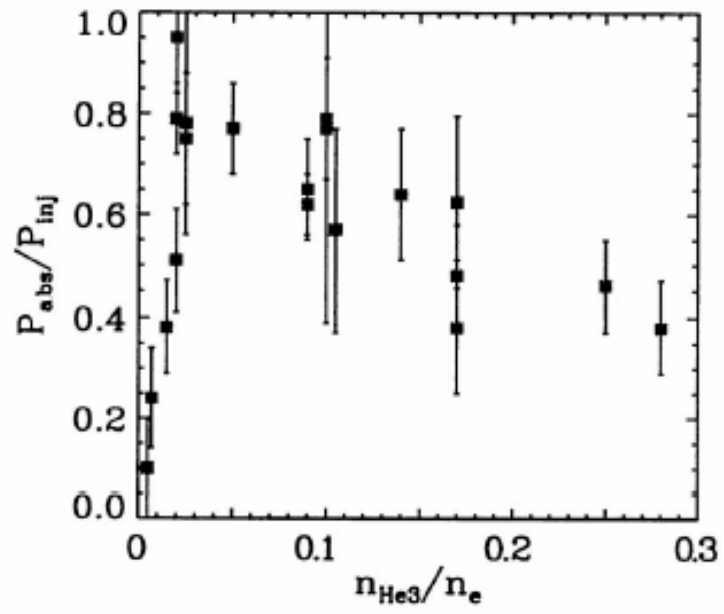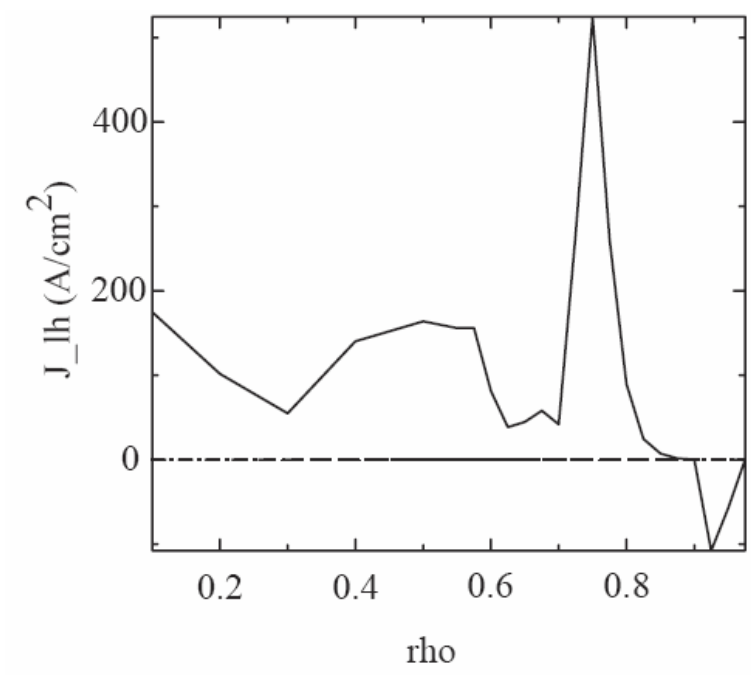
Figure 9
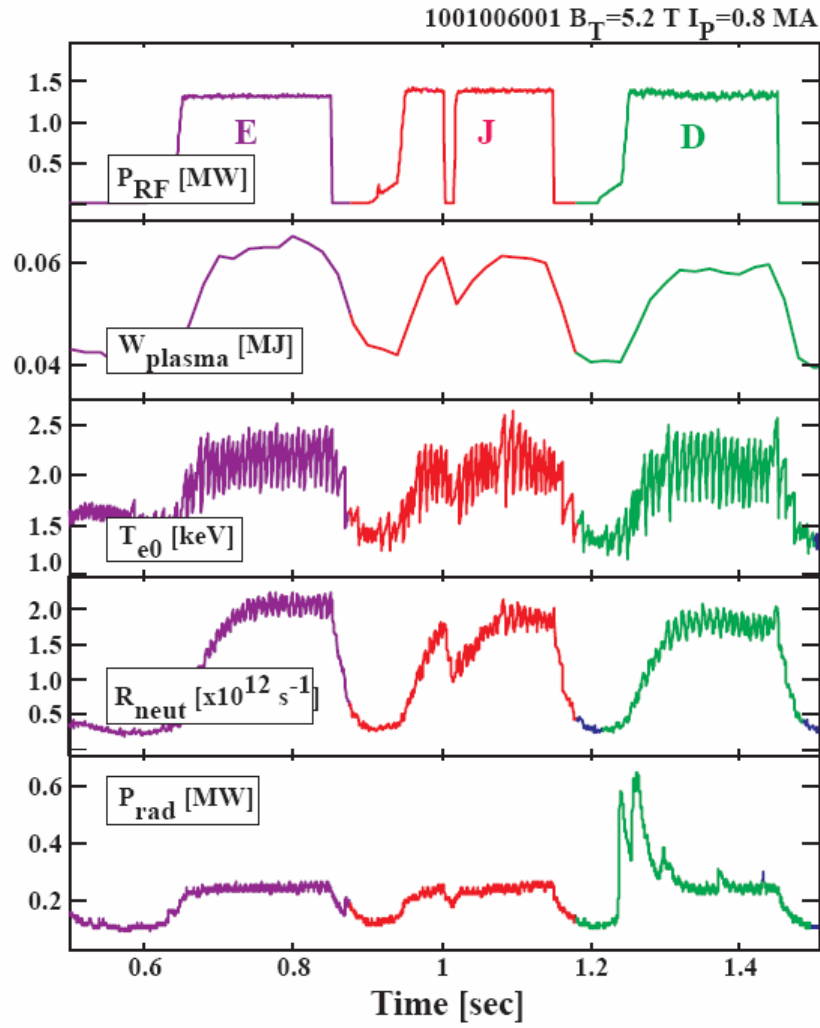
Figure 10

Figure 11

Shot 960117012
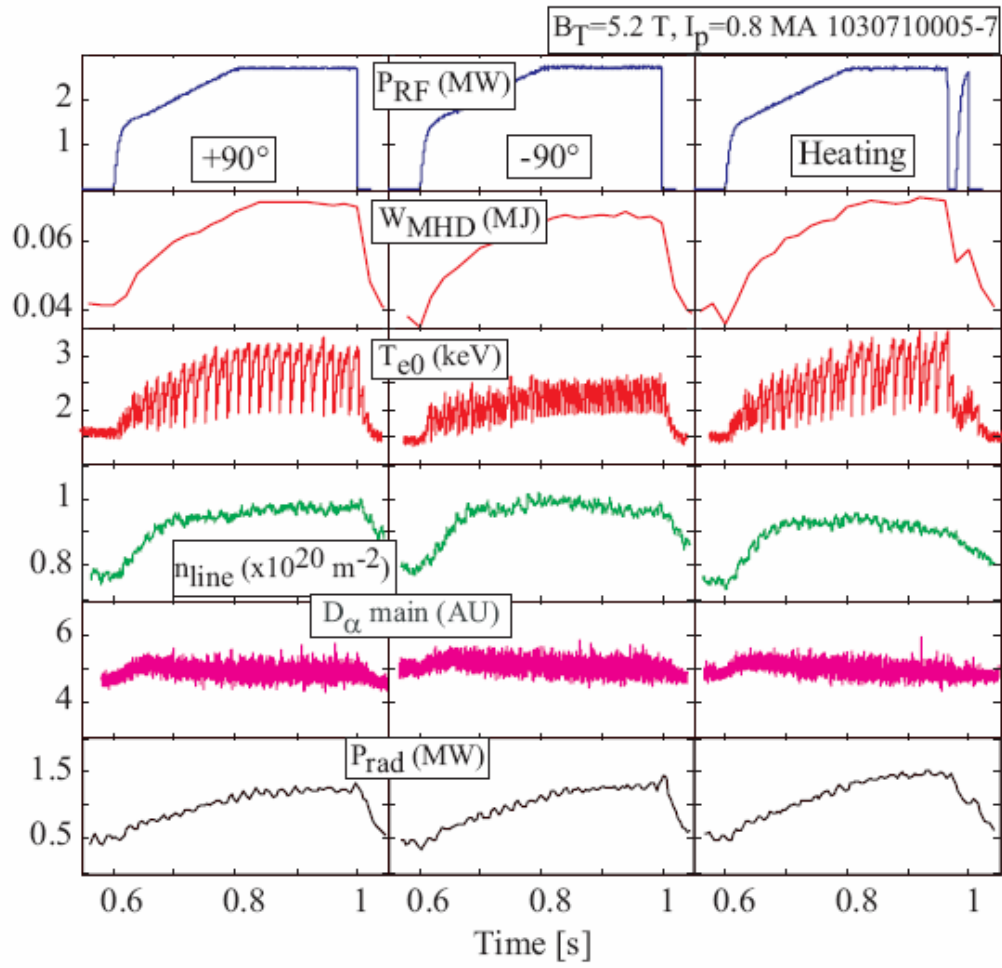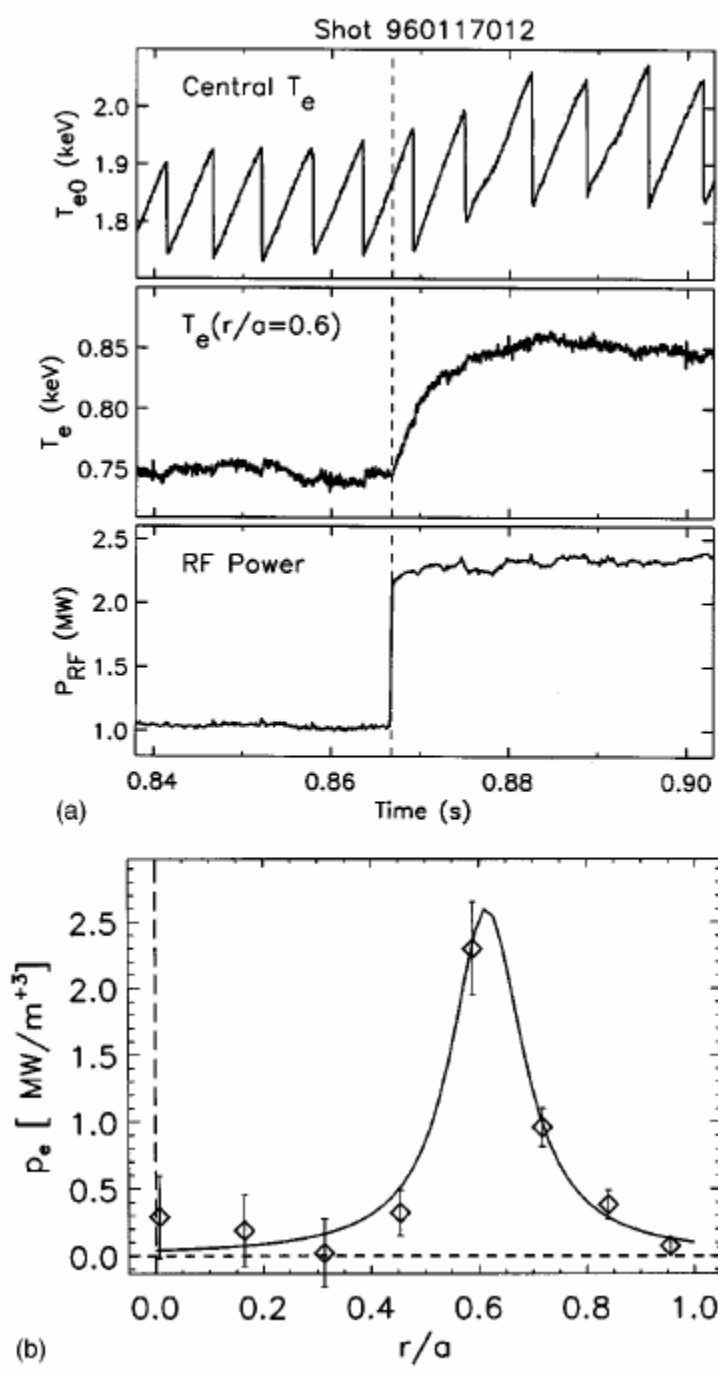
Figure 12(a,b)
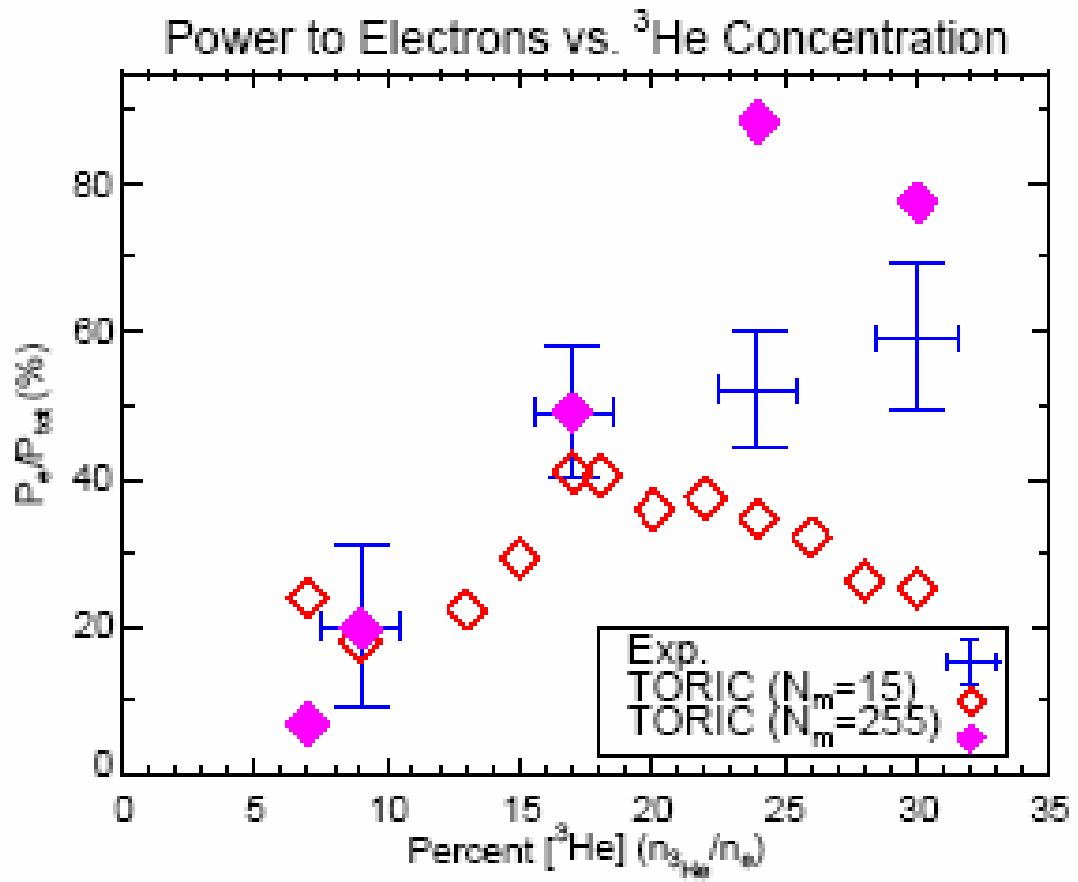
Figure 13
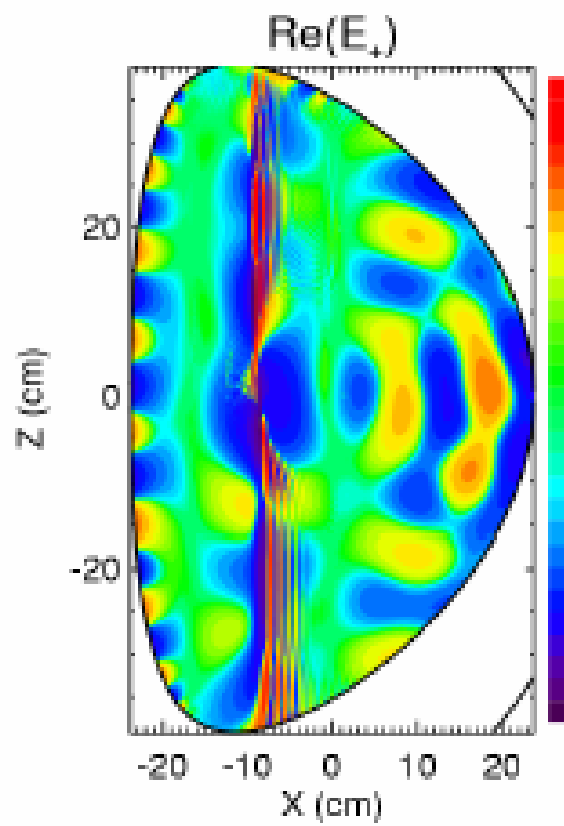
Figure 14: ICRF physics

Figure 15(a)

Figure 15(b)

Contour Plot of Fourier Analyzed PCI Data
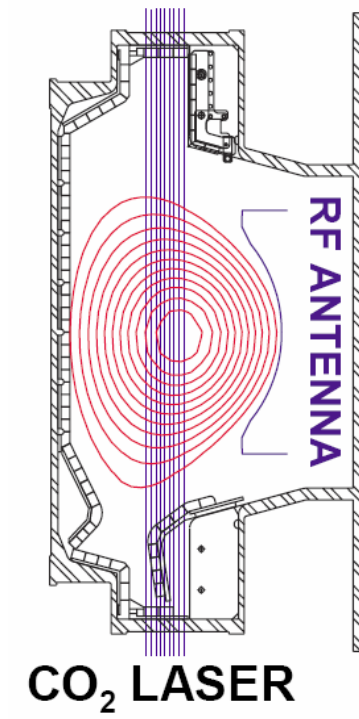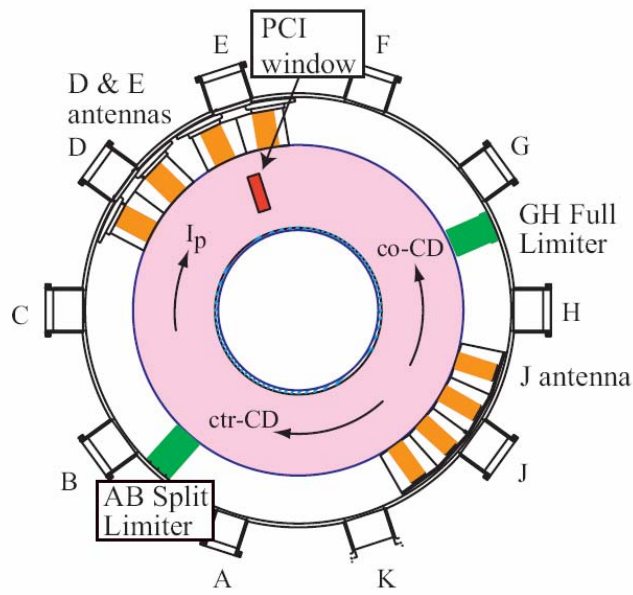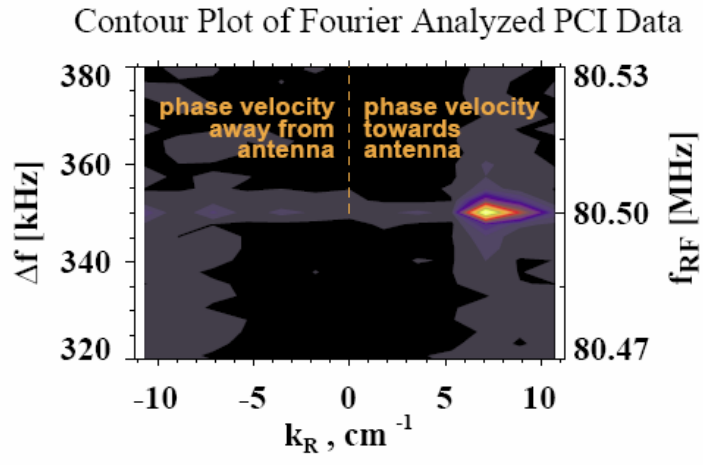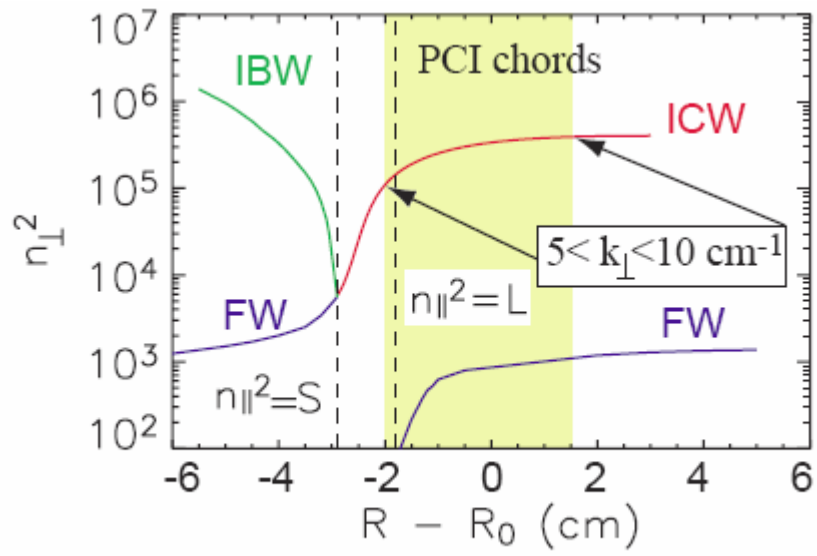
Figure 16(a)

Figure 16(b)

PCI Signal Structure
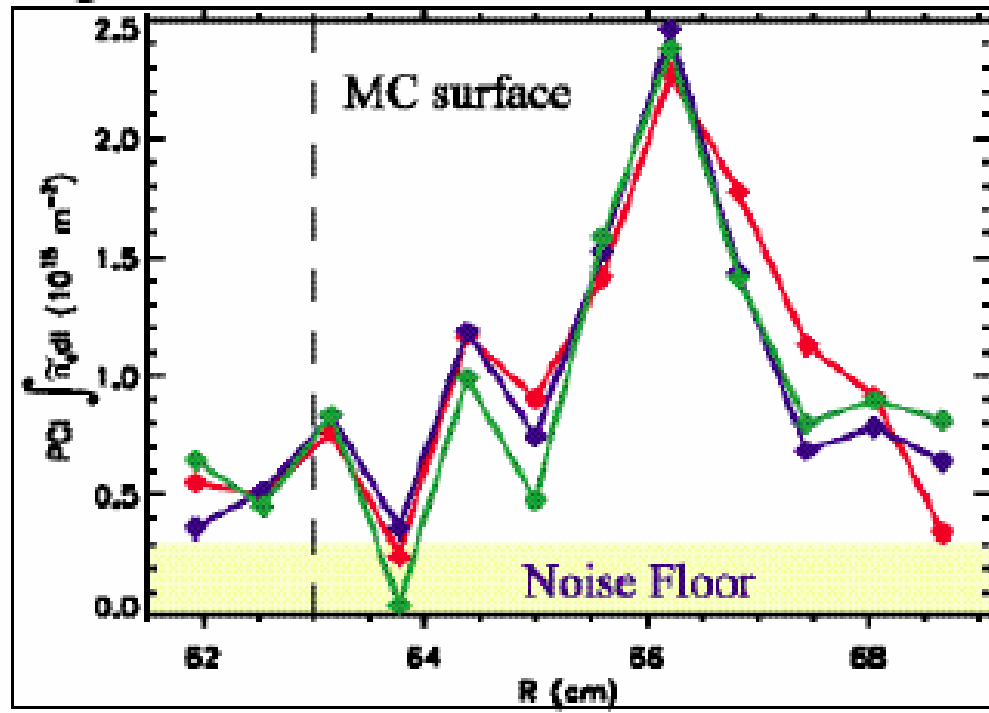
Figure 17

Figure 18

(a) Re(n_{e1})

(b) Re(n_{e1})
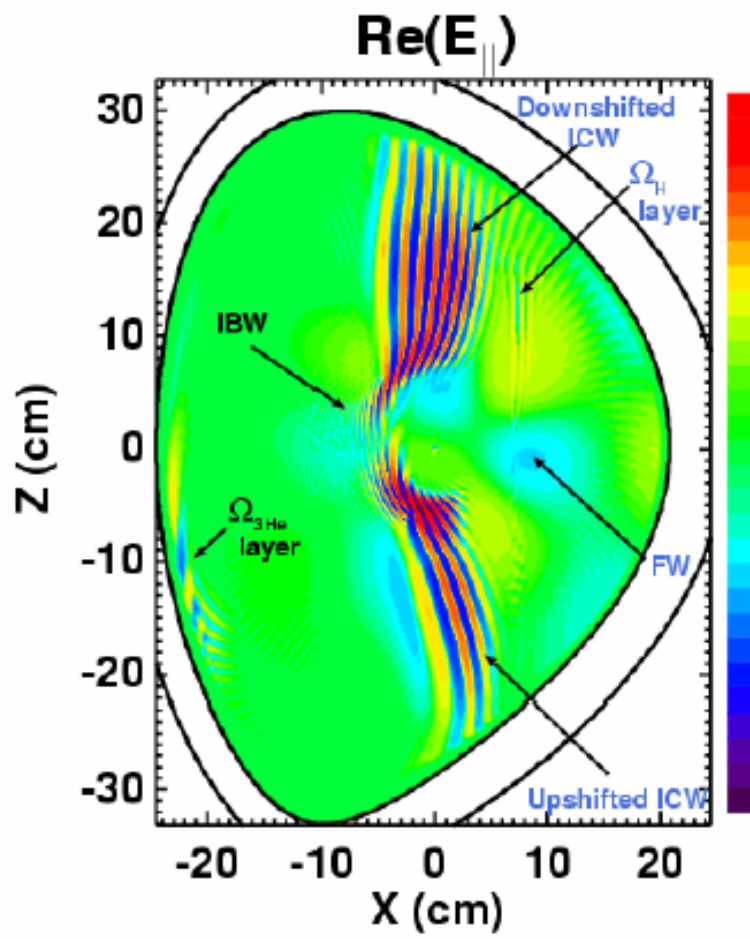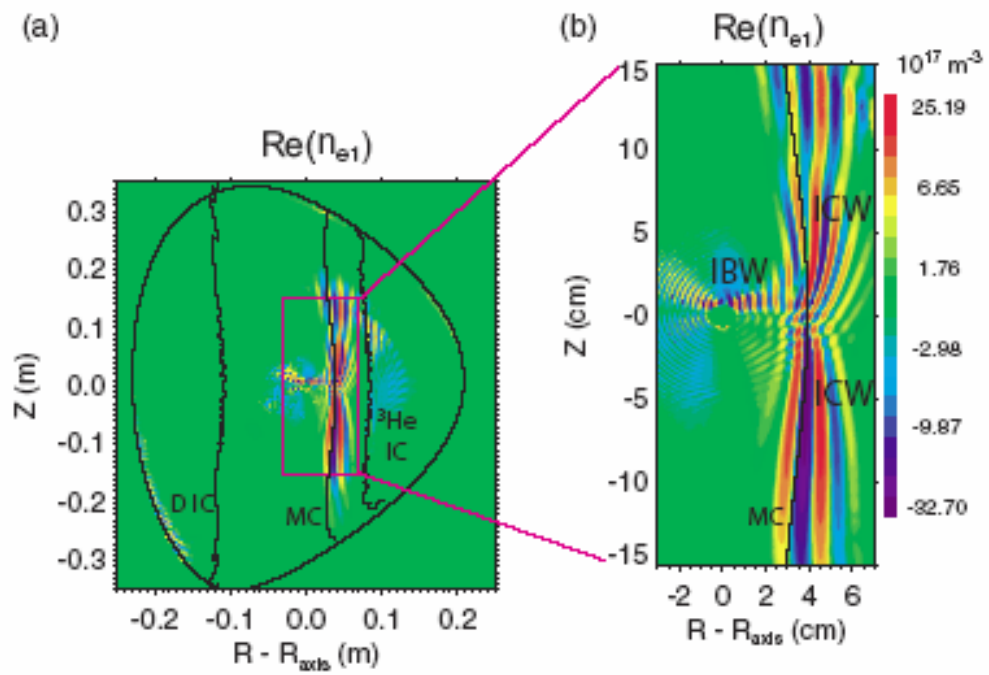
Figures 19(a,b)
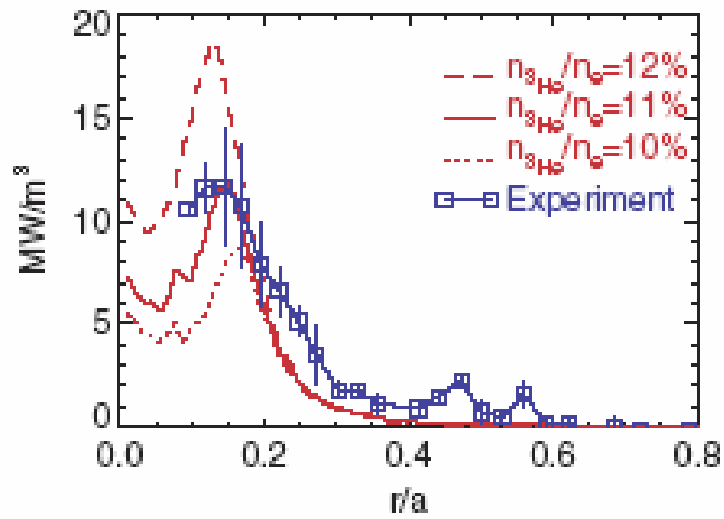
Figure 19(c)
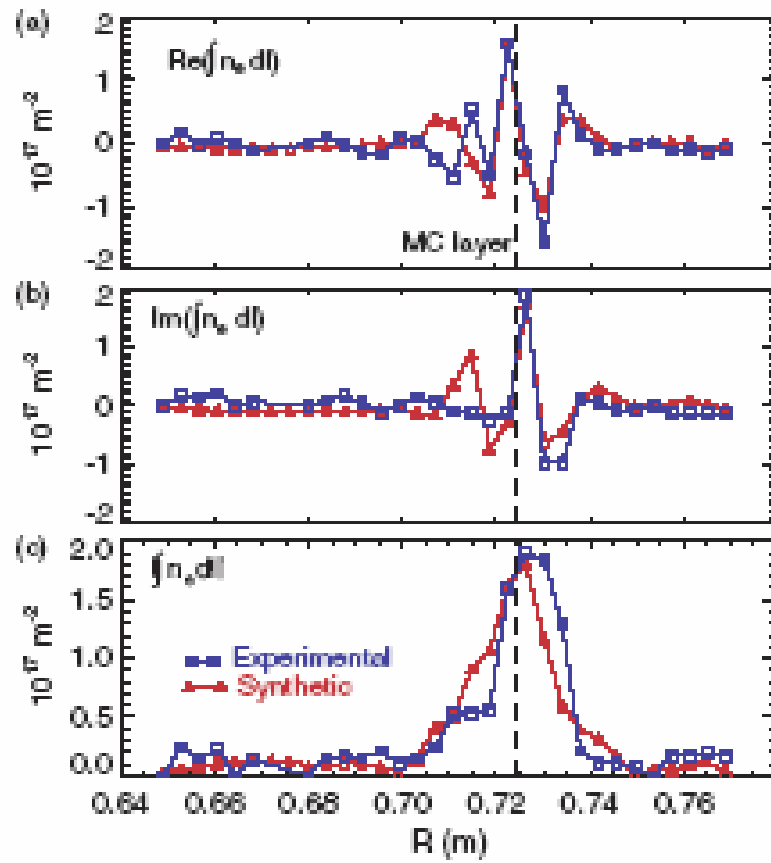
Figure 20
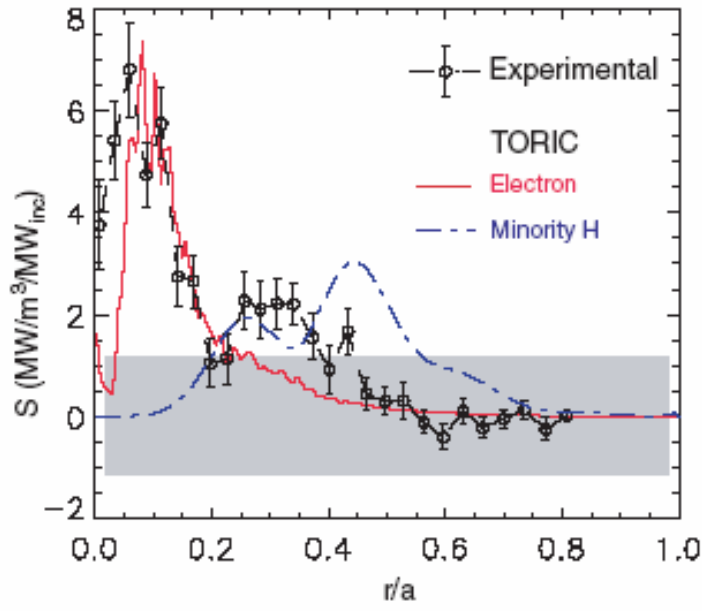
Figure 21(a)
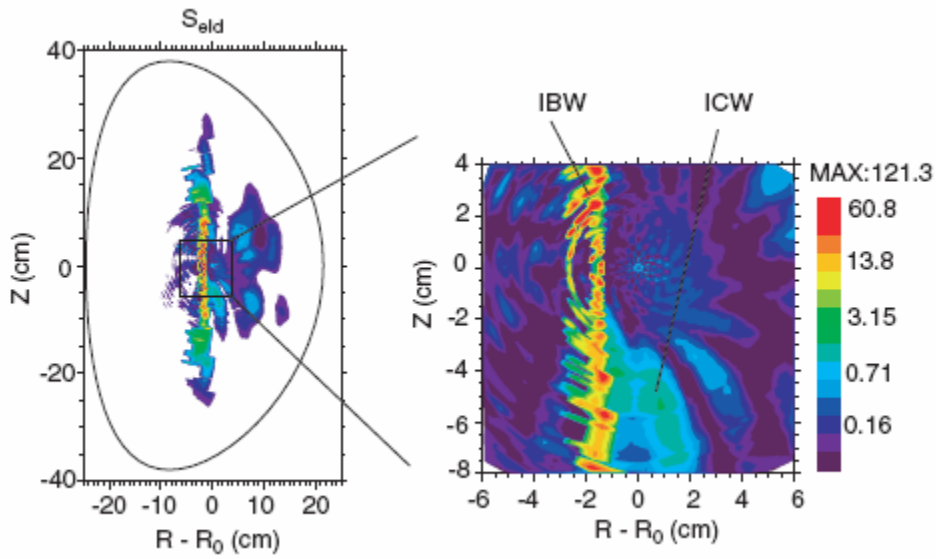
Figure 21(b)
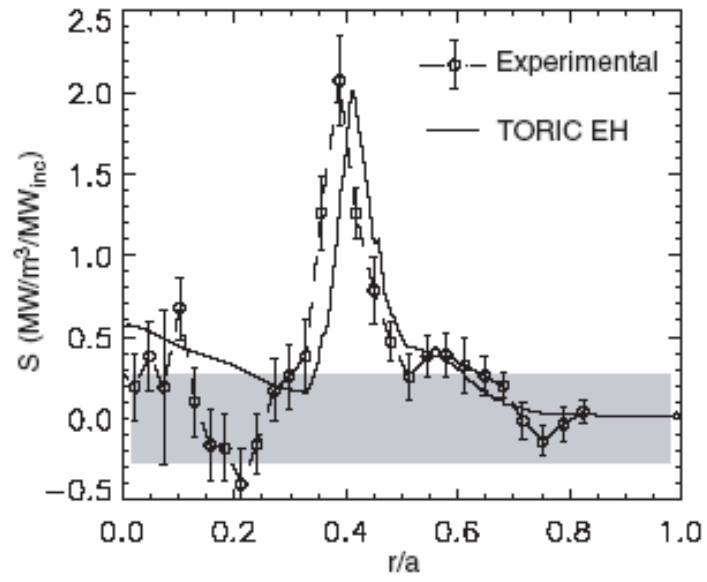
Figure 22(a)
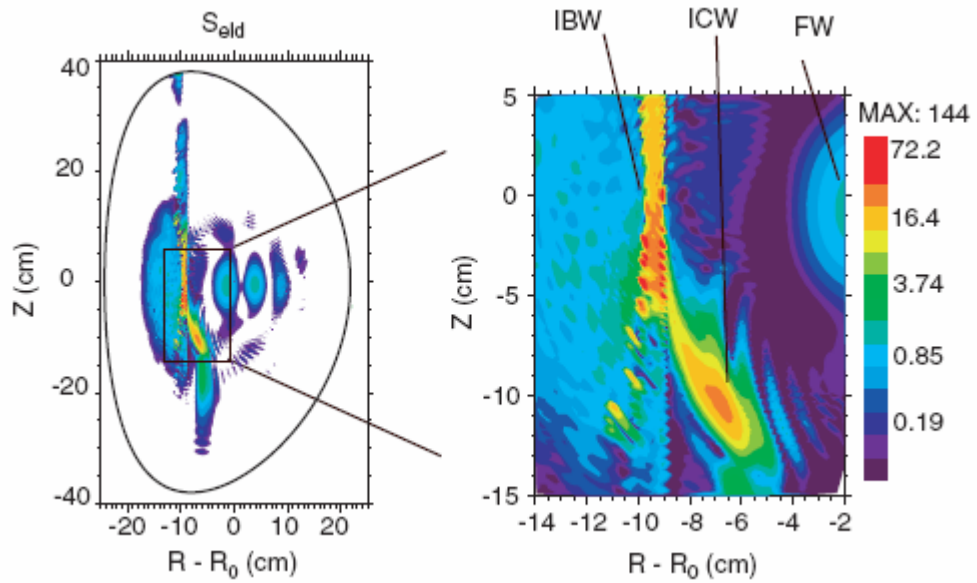
Figure 22(b)
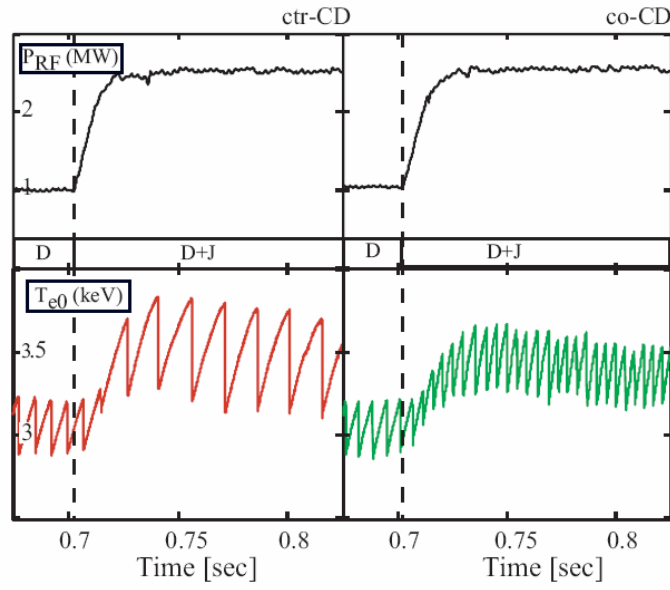
Figure 23(a)
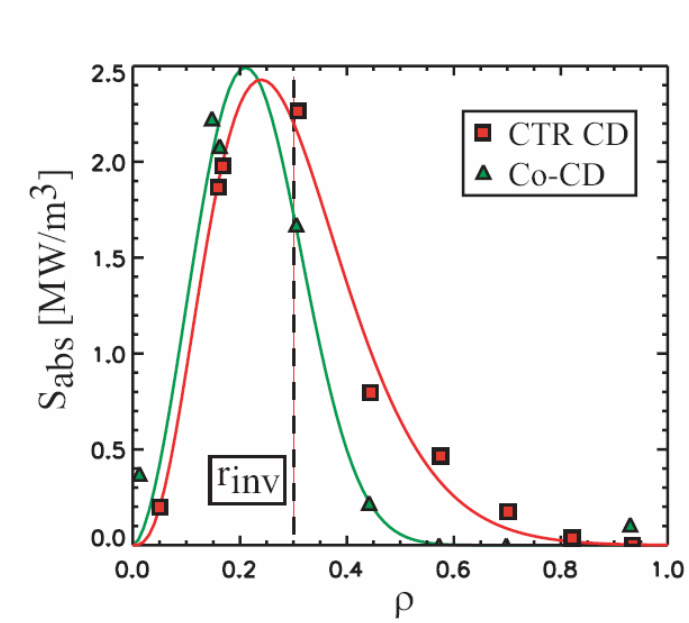
Figure 23(b)
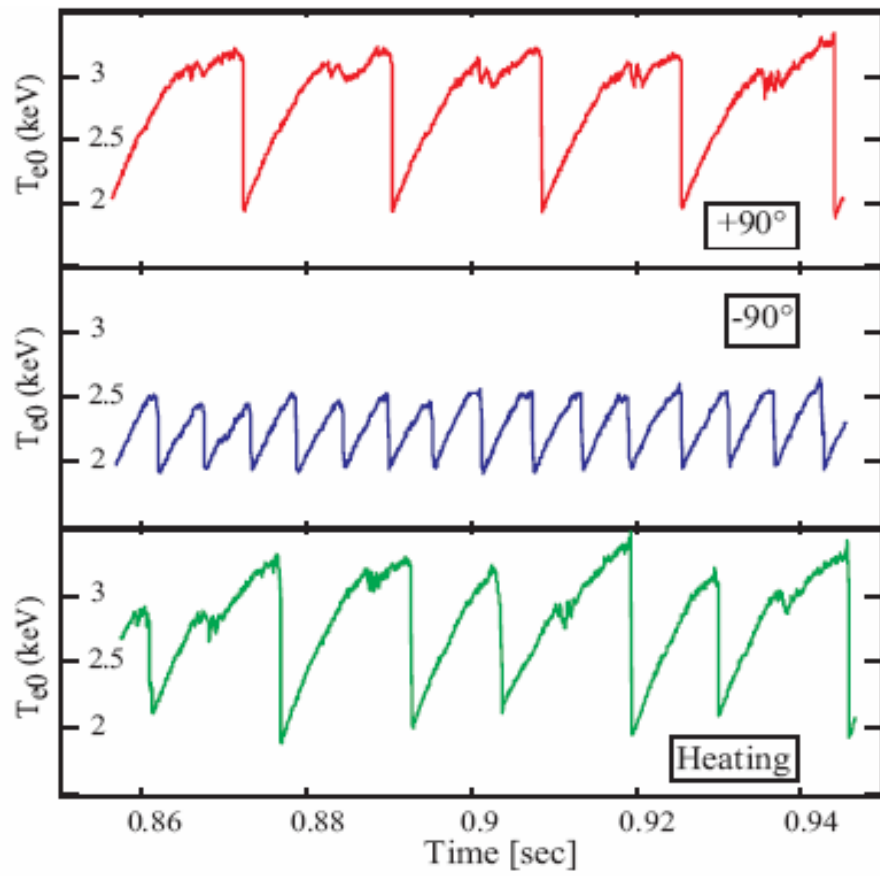
Figure 24
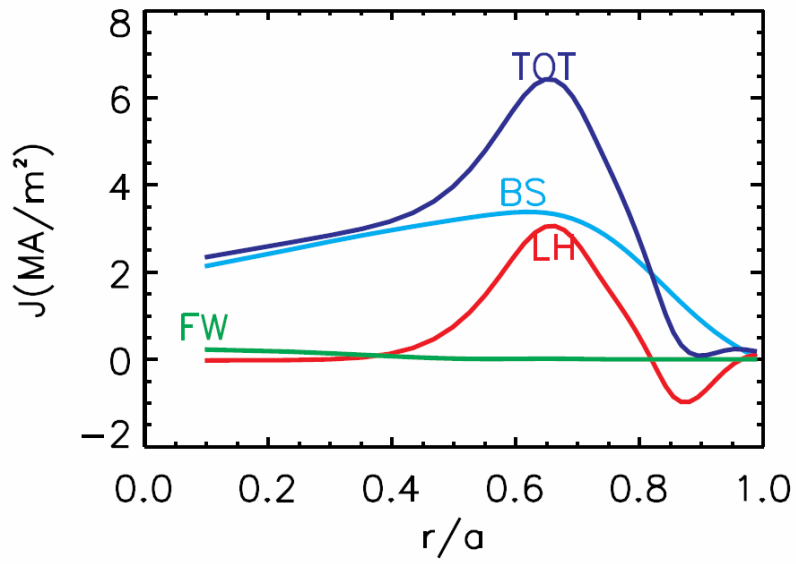
Figure 25(a)
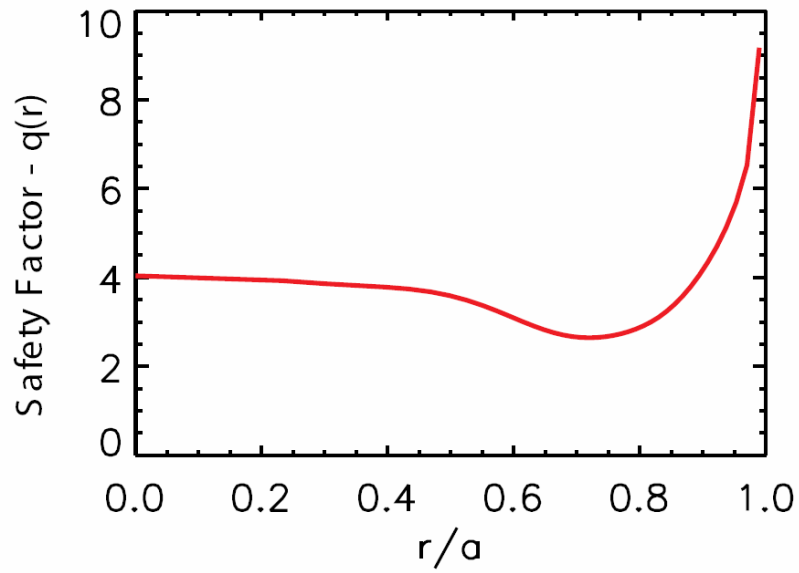
Figure 25(b)
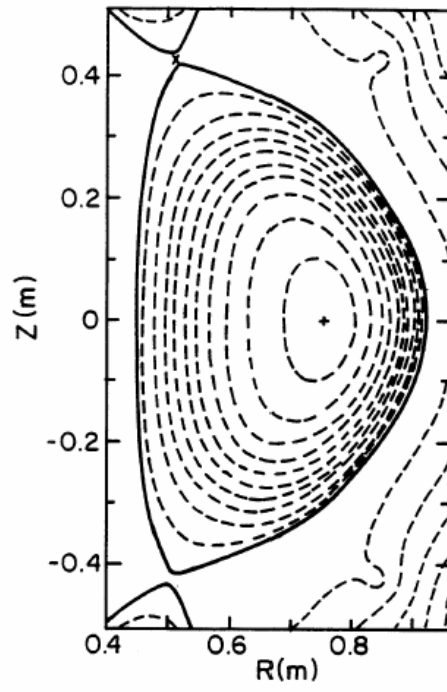
Figure 26
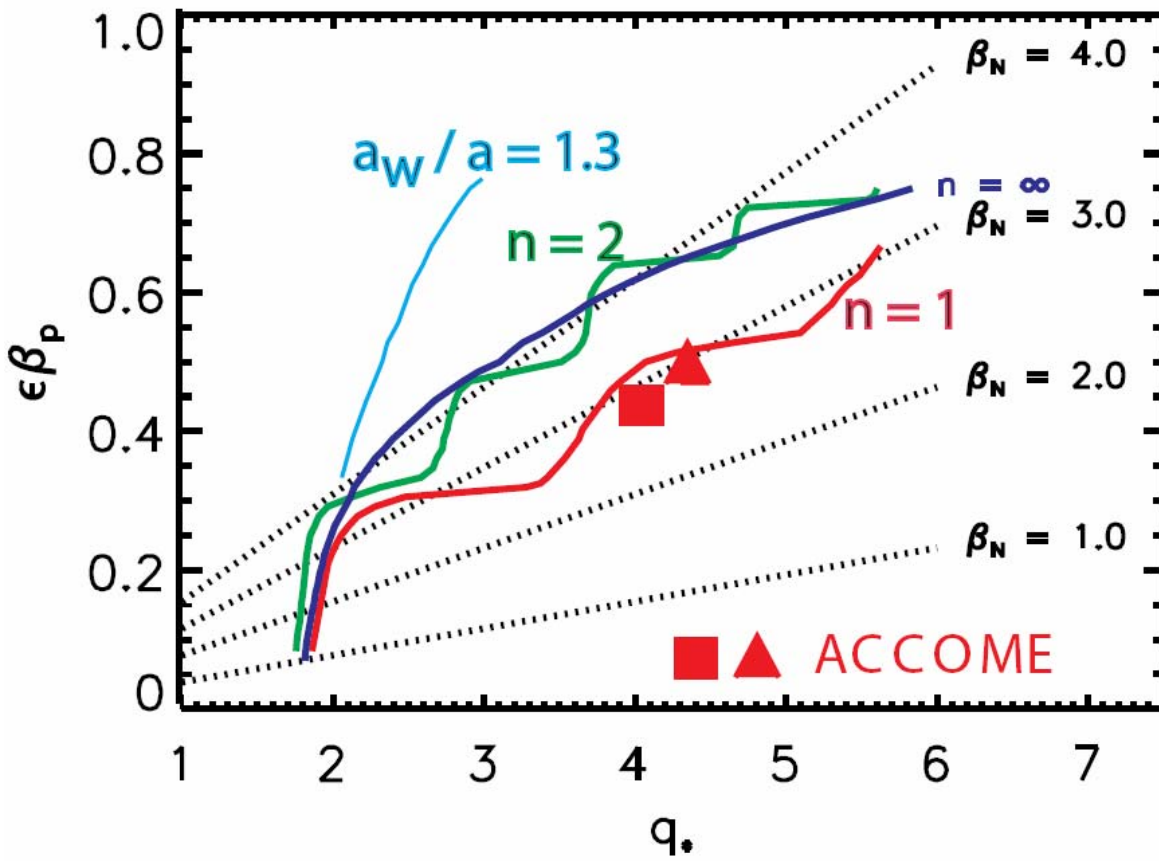
Figure 27
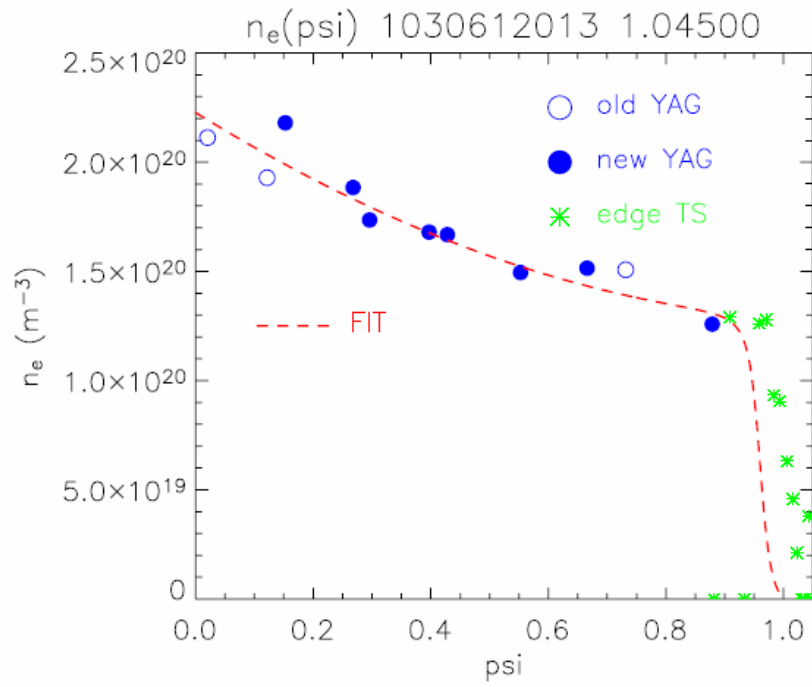
Figure 28(a)
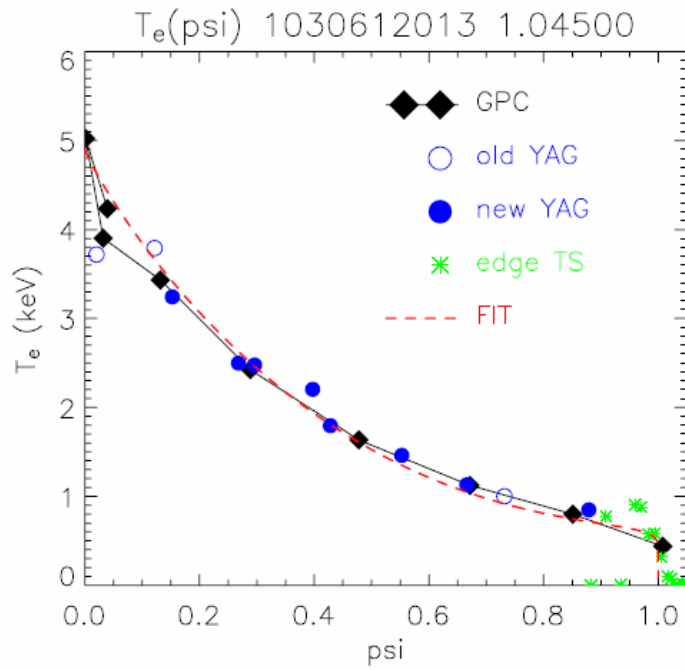
Figure 28(b)

Figure 29(a)

Figure 29(b)

Couplers (4)

Front
Waveguide
Assembly

Rear
Waveguide
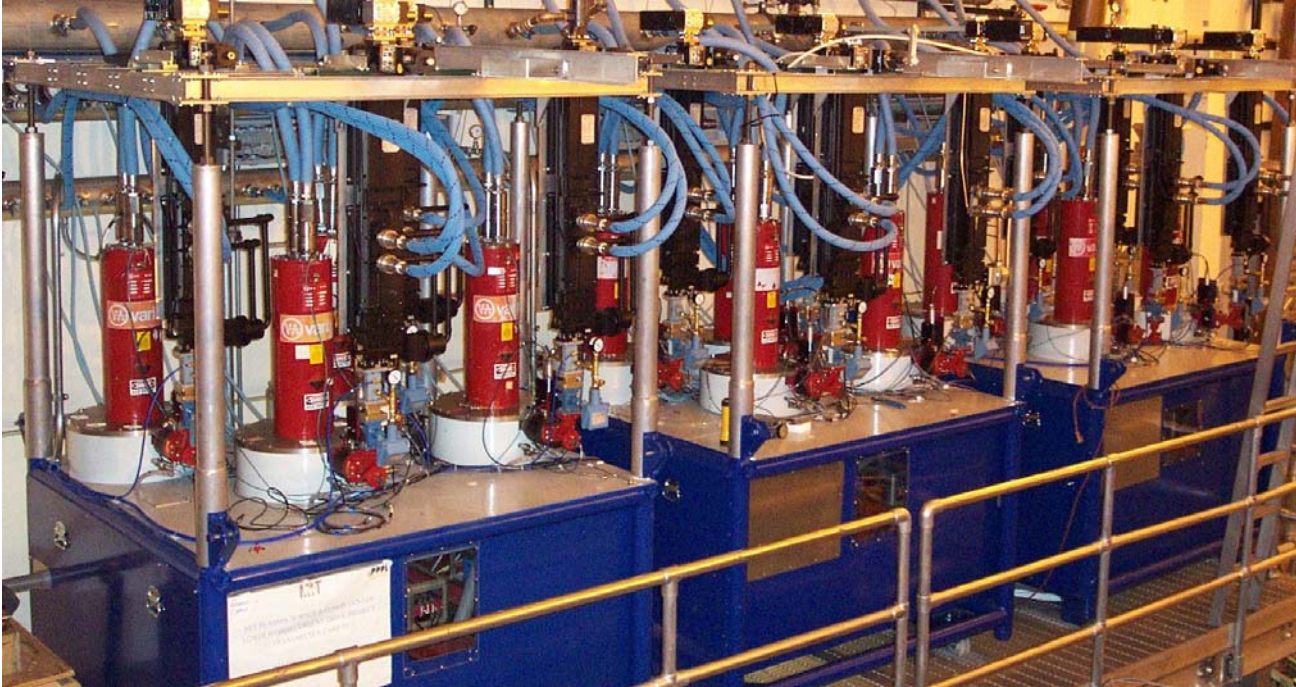Assembly

O-ring
Seal

Microwave
Windows

RF Gaskets

3 dB Power
Splitters

E plane
Transformers
22 to 5.5 mm
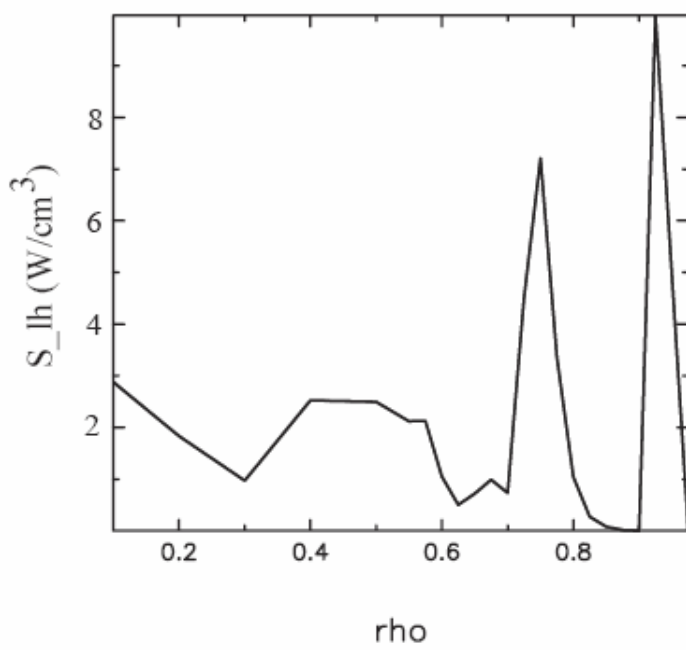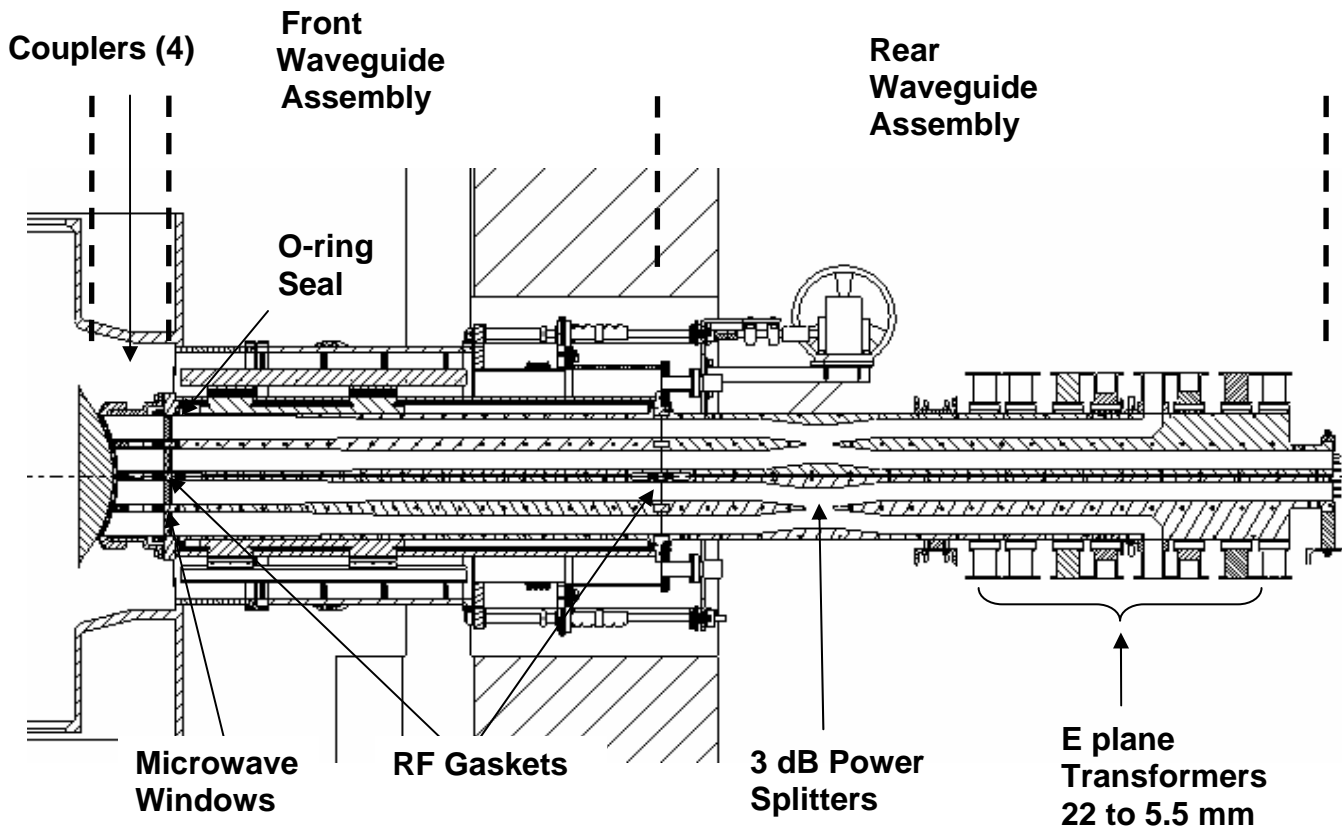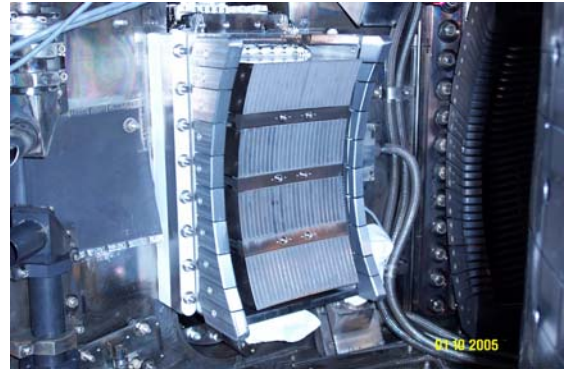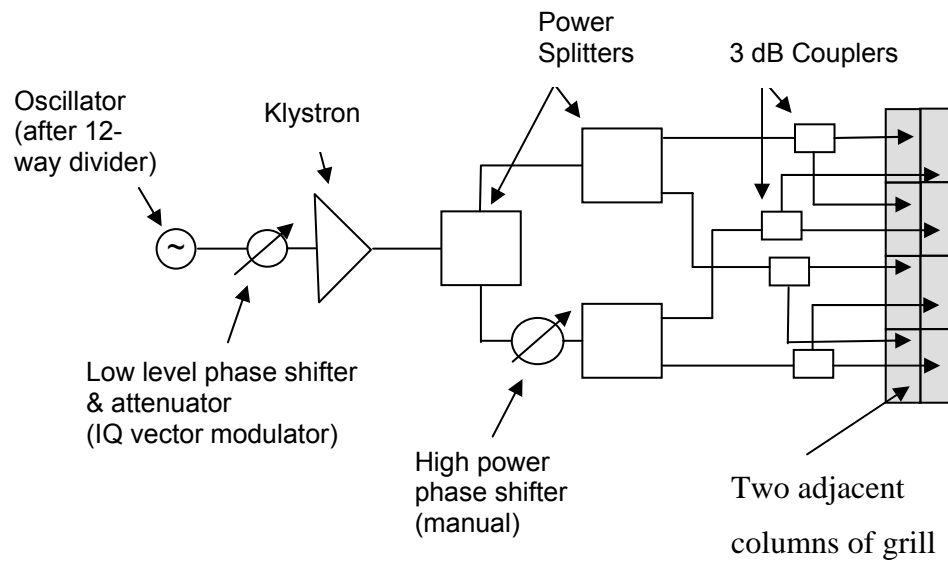
Figure 30

Figure 31

Figure 32

Figure 33

Figure 34
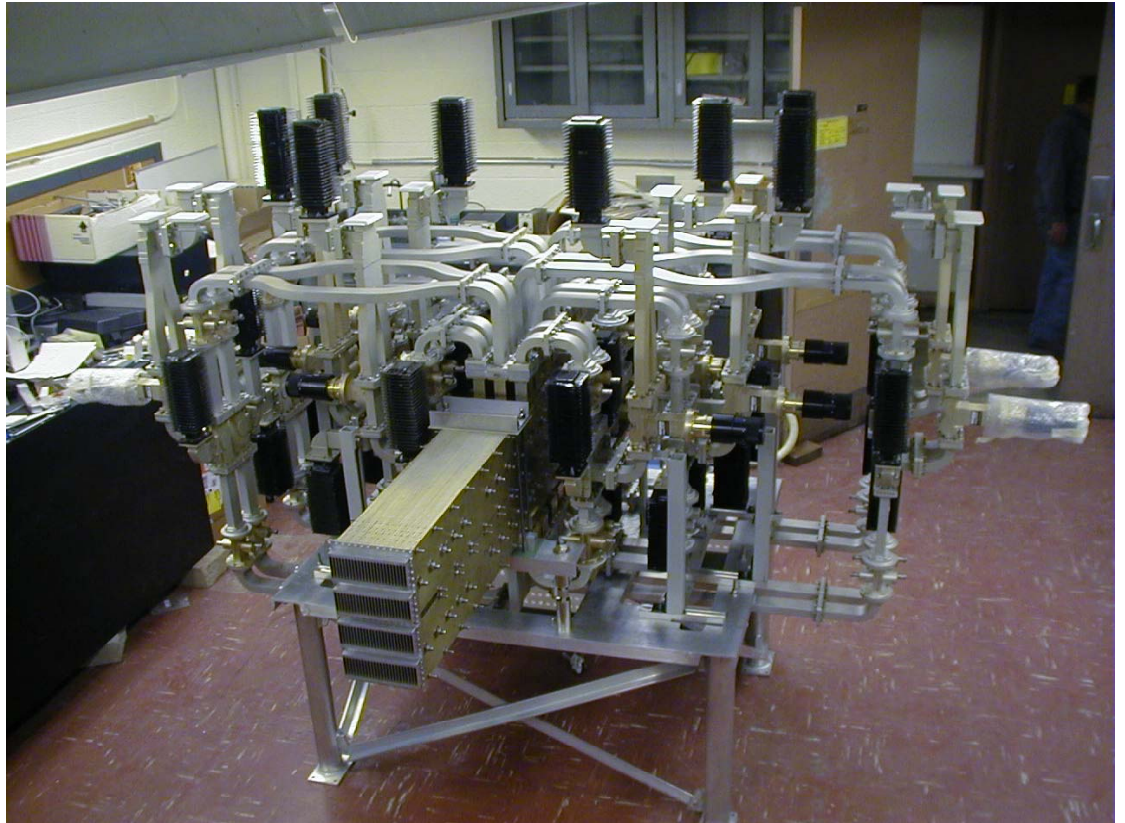
Figure 35
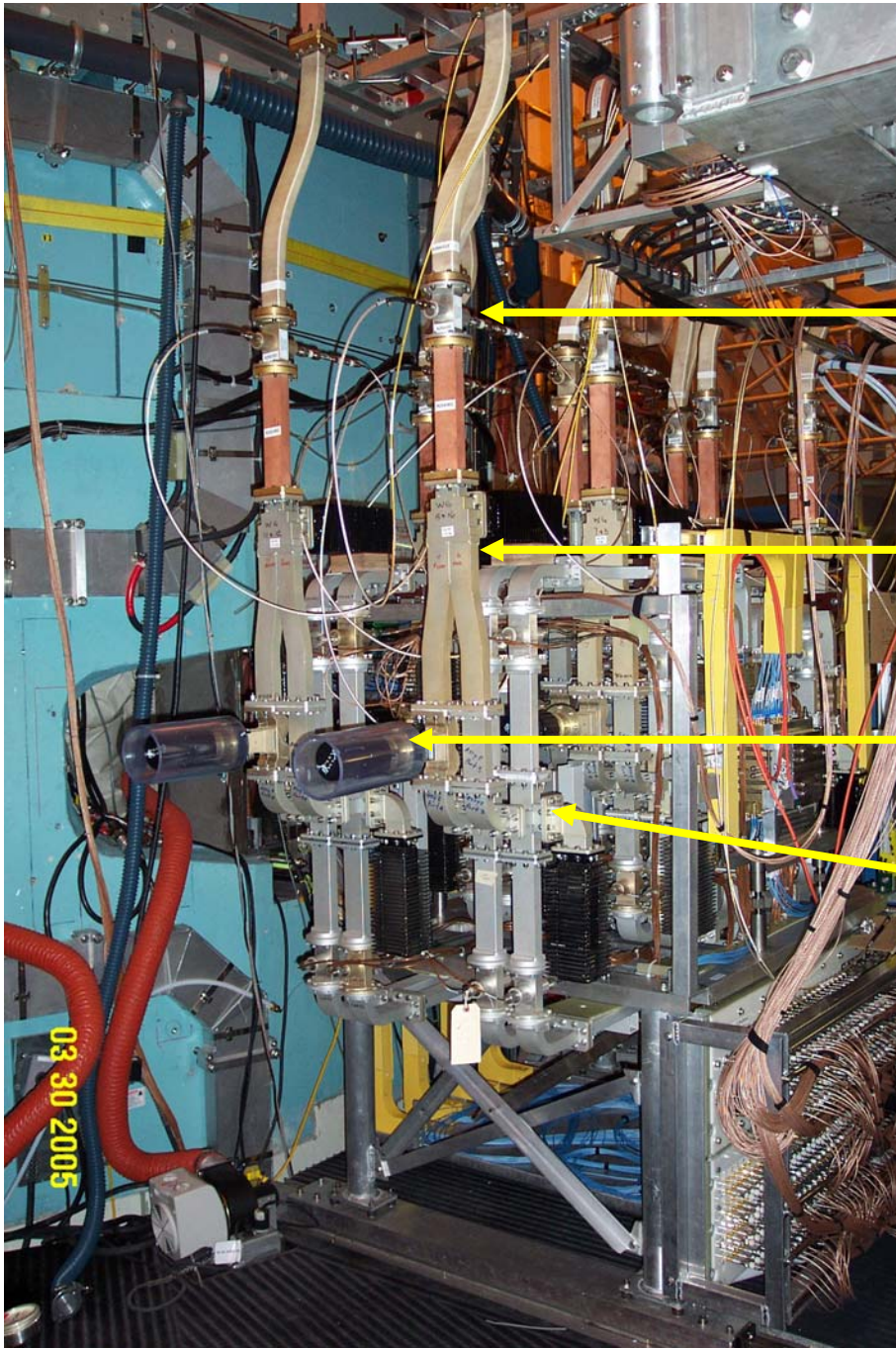
50 dB
directional
coupler

Splitter

Mechanical
Phase Shifter

Four-way Tee

Figure 36

Figure 37

Figure 38

Figure 39